Petroleum Science 23 (2026) 4662–4685

Contents lists available at ScienceDirect

Petroleum Science

journal homepage: www.keaipublishing.com/en/journals/petroleum-science

Original Paper

Characteristic reflection wave-equation traveltime inversion using full gradient

Cheng-Liang Wu [a,*], Bo Feng [b], Hua-Zhong Wang [b]

[a] College of Information Technology, Shanghai Ocean University, Shanghai, 201306, China
[b] Wave Phenomena and Intelligent Inversion Imaging Group (WPI), School of Ocean and Earth Science, Tongji University, Shanghai, 200092, China

A R T I C L E I N F O

Article history:
Received 20 October 2025
Received in revised form
24 February 2026
Accepted 15 April 2026
Available online 21 April 2026

Edited by Meng-Jiao Zhou

Keywords:
Characteristic reflection wavefield
Characteristic reflector structure
Full gradient
Velocity-reflectivity coupling

A B S T R A C T

With the advancement of oil and gas exploration into deepwater and deep formations, constructing accurate velocity models from reflection wave data has become essential for seismic imaging. The wave-equation-based reflection traveltime inversion (RTI) method typically decomposes the subsurface model into a smooth background velocity and high-wavenumber reflectors. In the Born modeling framework, both components jointly govern the generation of primary reflections. Conventional reflection-based inversion strategies often employ an alternating updating scheme to iteratively refine the background velocity and reflectivity. However, since reflectors are typically derived from migrated images that are themselves dependent on the current velocity model, this alternation can lead to inconsistencies between the updated reflectors and background velocity. In this paper, we propose a full-gradient RTI method based on the characteristic reflection wavefield (CRW). By using structural constraints from the characteristic reflectors and the imaging invariance of small-offset data, we derive the full gradient of the objective function with respect to the background velocity. The CRW enables robust measurement of traveltime shift and facilitates the construction of accurate adjoint source. The new gradient formulation comprises two key terms: A conventional reflection-based gradient term and a novel velocity-reflectivity coupling term. Numerical experiments demonstrate that the proposed full-gradient method effectively mitigates the coupling artifacts between the background velocity and reflectors during gradient computation, leading to improved gradient directions and significantly enhanced inversion convergence.

1. Introduction

Full waveform inversion (FWI) has become a powerful tool for constructing high-resolution velocity model in seismic imaging (Tarantola, 1984). By minimizing the misfit between observed and simulated seismic data, FWI formulates an L_2-norm objective function that maps waveform differences back to the subsurface, enabling iterative updates of the velocity model. However, FWI is highly sensitive to the initial velocity model and is prone to convergence toward local minima. Numerous methods have been proposed to improve its stability and robustness (Bunks et al., 1995; Lee and Kim, 2003; Virieux and Operto, 2009; Fichtner et al., 2013; Zhou et al., 2015; Li and Demanet, 2016; Hu et al., 2017; Huang et al., 2017; Qu et al., 2017; Zhang et al., 2017; Chen et al., 2018, 2020; Liu et al., 2018; Xie et al., 2024; Wang et al., 2024; Borisov et al., 2025).

FWI has achieved considerable success in building velocity models at shallow to intermediate depths, particularly through the use of diving wave and refraction, which provide robust constraints on the velocity model (Zhou et al., 2015; Abreo et al., 2018; da Silva et al., 2024). However, these waves have limited penetration depth, making them ineffective for updating deep or ultra-deep velocity models. To overcome this limitation, researchers have proposed FWI approaches based on reflections, which carry deeper subsurface information and therefore offer significant potential for high-accuracy deep velocity model building (Xu et al., 2012a, 2012b; Wang et al., 2013; Sun et al., 2016; Yao et al., 2020; Yang et al., 2020; Zhang et al., 2025).

* Corresponding author.
E-mail address: wuchengliang1990@163.com (C.-L. Wu).
Peer review under the responsibility of China University of Petroleum (Beijing).

https://doi.org/10.1016/j.petsci.2026.04.026
1995-8226/

In reflection FWI (RFWI), the conventional FWI gradient contains both low-wavenumber wave path information and high-wavenumber migration isochrons. Since the amplitude of the migrated component is typically an order of magnitude larger than that of the wave path term (Yao et al., 2020), the gradient tends to be dominated by high-wavenumber updates, thereby increasing the risk of convergence to local minima. To address this issue and effectively recover the low-wavenumber background, two main strategies have been developed: (1) implicit methods, which suppress high-wavenumber components through wavefield decomposition or angle-domain filtering, thereby preserving only the low-wavenumber wave path information (Alkhalifah, 2014; Kazei et al., 2016; Irabor and Warner, 2016; Ramos-Martinez et al., 2016; Nie et al., 2025); and (2) explicit methods, which decompose the velocity model into a smooth background velocity model and high-wavenumber reflectivity, and then invert these components separately using reflection waveform inversion (RWI) (Xu et al., 2012a, 2012b; Wang et al., 2013; Sun et al., 2016; Yao et al., 2020).

RWI typically employs a Born-linearized forward operator to simulate primary reflections. This operator assumes that seismic waves propagate through a background velocity model, scatter at reflectors, and are recorded at receiver locations. As a result, the traveltimes of the reflections are jointly influenced by both the background velocity and the reflector geometry. A common inversion strategy is to alternately update the background velocity and reflectivity. However, this sequential process—particularly when the reflectors are held fixed during velocity updates—often introduces inconsistencies between the velocity model and the reflectors, thereby hindering convergence and reducing inversion accuracy.

Van Leeuwen and Mulder (2009) proposed the variable projection method, in which the normal equations for the reflectivity are substituted back into the inversion process, allowing the velocity model to be updated independently. While theoretically efficient, this approach requires the construction of accurate projection operators, which are computationally expensive in practice and therefore often approximated. Plessix et al. (2012) introduced an inversion scheme in the pseudo-time domain to mitigate velocity-depth coupling. Brossier et al. (2015) proposed the use of a reflection sensitivity kernel under the assumption of a known reflector and highlighted the importance of maintaining reflector invariance through the velocity model. Chavent et al. (2014), Chavent (2017) and Tcheverda et al. (2016) developed a reflection FWI algorithm within the migration based travel time (MBTT) framework by incorporating a time-domain representation of reflectivity, thereby reducing its dependence on the background velocity. Kryvohuz et al. (2019) suggested incorporating reflectivity into the data space to ensure dynamic consistency using a least-squares criterion. However, this approach involves significant computational cost. Valensi et al. (2017) and Baina and Valensi (2018) analyzed the inconsistencies that arise from alternately updating reflectivity and background velocity in RWI. Valensi and Baina (2019) derived a consistency gradient linking velocity and reflectivity, but did not provide a concrete implementation. Valensi and Baina (2021) further proposed a consistency gradient formulation based on time alignment within the velocity model using zero-offset data, aiming to address the coupling between velocity and reflectivity. Hassine et al. (2022) addressed this issue within a one-way wavefield framework, proposing a one-way waveform inversion (OWI) methodology, which was subsequently demonstrated on real marine seismic data (Hassine et al., 2024).

In reflection-based velocity inversion, the Hessian operator plays a critical role in characterizing second-order sensitivity and parameter coupling between background velocity and reflector geometry, and thus provides the theoretical basis for mitigating velocity-depth ambiguity and improving convergence. Xu et al. (2021) derived the Hessian of reflection waveform inversion under the Born approximation and demonstrated that Hessian-based Gauss-Newton optimization significantly enhances low-to intermediate-wavenumber velocity recovery. Wang et al. (2021) further analyzed the functional Hessian of reflection FWI and implemented a second-order adjoint-state Gauss-Newton scheme, showing improved convergence and resolution for deep velocity model building. Assis et al. (2024) investigated the tomographic Hessian in inversion velocity analysis and demonstrated that incorporating second-order information effectively reduces parameter trade-offs and stabilizes background velocity updates in reflection-dominated settings. In addition to explicit Hessian formulations, several studies have focused on understanding and approximating Hessian effects to improve practical feasibility. Alkhalifah and Wu (2016) proposed model-space filtering strategies that implicitly reshape the gradient to mimic inverse Hessian effects, thereby enhancing background velocity updates without explicitly constructing the Hessian. More recently, Abolhassani et al. (2025) incorporated a depth-dependent Hessian preconditioner into one-way reflection FWI, achieving improved stability and computational efficiency without explicitly forming the full Hessian. Despite the demonstrated effectiveness of Hessian-based and second-order reflection inversion methods, their practical implementation remains challenged by high computational cost and strong reliance on accurate reflectivity or modeling assumptions.

In this paper, we propose a characteristic reflection wave-equation traveltime inversion method based on full-gradient computation. The remainder of this paper is organized as follows. First, we review conventional reflection-based velocity inversion method, in which reflectivity and velocity are iteratively updated due to their inherent coupling. We then explain the necessity of using full gradient to achieve more consistent and accurate velocity model updates. Next, based on cross-correlation traveltime shift measurements and by leveraging the imaging invariance of small-offset reflection data, we derive a full-gradient reflection traveltime inversion framework and establish a gradient formulation based on the two-way wave equation. This method is then extended under the characteristic reflection wavefield paradigm, from which we derive a corresponding full-gradient expression for background velocity. By incorporating structural constraints from characteristic reflectors, the proposed approach enables robust traveltime shift measurements and accurate gradient calculations. Finally, numerical experiments are presented to validate the effectiveness and advantages of the proposed method.

2. Conventional reflection-based velocity inversion method

In reflection-based velocity inversion method, the background velocity is updated using primary reflections. The associated misfit function can be written as:

$$\begin{aligned} \min_{m_s(\mathbf{x})} \ & \mathscr{J}\left(m_s(\mathbf{x})\right) = \ell\left(d_{obs}(\mathbf{x}_r, t, \mathbf{x}_s), d_{cal}(\mathbf{x}_r, t, \mathbf{x}_s)\right) \\ \text{s.t.} \ & d_{cal}(\mathbf{x}_r, t, \mathbf{x}_s) = \mathbf{C}[\mathbf{B}(m_s(\mathbf{x}))R(\mathbf{x})] \end{aligned}, \tag{1}$$

where $\mathbf{x}_s$ and $\mathbf{x}_r$ denote the source and receiver positions, respectively, t is time, $\mathbf{d}_{cal} \equiv d_{cal}(\mathbf{x}_r, t, \mathbf{x}_s)$ and $\mathbf{d}_{obs} \equiv d_{obs}(\mathbf{x}_r, t, \mathbf{x}_s)$ are the simulated and observed seismic data, respectively. The operator ℓ denotes a norm that measures the difference between observed and simulated data, which is typically chosen as the L_2-

norm $\ell = \|\cdot\|^2$, $\mathbf{B}(\cdot)$ denotes the forward modeling operator, which depends on the velocity model $\mathbf{m}_s \equiv m_s(\mathbf{x})$ and reflectivity $\mathbf{R} \equiv R(\mathbf{x})$. $\mathbf{C}[\cdot]$ represents the sampling operator that maps the wavefield to the receiver positions.

According to the wave-equation-based demigration formulation (Eq. (B.4)), the reflection wavefield $\mathbf{d}_{\mathrm{cal}}$ can be expressed as,

$$\begin{aligned} u_{\mathrm{cal}}(\mathbf{x}_r, t, \mathbf{x}_s) &= -\int R(\mathbf{x}) \frac{\partial^2 u_0(\mathbf{x}, t, \mathbf{x}_s)}{\partial t^2} * g_0(\mathbf{x}, t, \mathbf{x}_r) \mathrm{d}\mathbf{x} \\ d_{\mathrm{cal}}(\mathbf{x}_r, t, \mathbf{x}_s) &= \mathbf{C}[u_{\mathrm{cal}}(\mathbf{x}_r, t, \mathbf{x}_s)] \end{aligned}, \tag{2}$$

where $\mathbf{u}_0 \equiv u_0(\mathbf{x}, t, \mathbf{x}_s)$ is the background wavefield propagated from the source position $\mathbf{x}_s$ to the subsurface point $\mathbf{x}$, and $\mathbf{g}_0 \equiv g_0(\mathbf{x}, t, \mathbf{x}_r)$ is the Green's function from point $\mathbf{x}$ to the receiver position $\mathbf{x}_r$. The * represents convolution.

Eq. (1) and Eq. (2) show that the modeled data $\mathbf{d}_{\mathrm{cal}}$ is a nonlinear function of the background velocity $\mathbf{m}_s$. The simulated data is jointly dependent on the background velocity $\mathbf{m}_s$ and the reflector image $\mathbf{R}$. However, during the velocity inversion process, the reflectivity is unknown and must be estimated. Thus, the misfit function in Eq. (1) is reformulated as

$$\min_{m_s(\mathbf{x}), R(\mathbf{x})} \mathcal{J}(m_s(\mathbf{x}), R(\mathbf{x})) = \ell(d_{\mathrm{obs}}(\mathbf{x}_r, t, \mathbf{x}_s), d_{\mathrm{cal}}(\mathbf{x}_r, t, \mathbf{x}_s)). \tag{3}$$

A conventional approach to solving Eq. (3) is through sequential inversion, where only one variable is updated at a time. This process can be described as follows, First, given a background velocity model $\mathbf{m}_s$, the reflectivity $\tilde{\mathbf{R}}$ is estimated (Eq. (4a)). Using this updated reflectivity, reflections are modeled via Eq. (2), and then the background velocity $\tilde{\mathbf{m}}_s$ is updated by minimizing the misfit between observed and simulated data (Eq. (4b)). This process is iterated to gradually update the velocity model,

$$\begin{aligned} \tilde{R}(\mathbf{x}) &= \arg\min_{R(\mathbf{x})} \mathcal{J}(R(\mathbf{x})) = \ell(d_{\mathrm{obs}}(\mathbf{x}_r, t, \mathbf{x}_s), d_{\mathrm{cal}}(\mathbf{x}_r, t, \mathbf{x}_s)) \\ \text{s.t. } & d_{\mathrm{cal}}(\mathbf{x}_r, t, \mathbf{x}_s) = \mathbf{CB}(m_s(\mathbf{x}))R(\mathbf{x}) \end{aligned}, \tag{4a}$$

$$\begin{aligned} \tilde{m}_s(\mathbf{x}) &= \arg\min_{m_s(\mathbf{x})} \mathcal{J}(m_s(\mathbf{x})) = \ell(d_{\mathrm{obs}}(\mathbf{x}_r, t, \mathbf{x}_s), d_{\mathrm{cal}}(\mathbf{x}_r, t, \mathbf{x}_s)) \\ \text{s.t. } & d_{\mathrm{cal}}(\mathbf{x}_r, t, \mathbf{x}_s) = \mathbf{CB}(m_s(\mathbf{x}))\tilde{R}(\mathbf{x}) \end{aligned}. \tag{4b}$$

From Eq. (4a) and Eq. (4b), it is evident that the velocity update is performed under the assumption of a fixed reflectivity. However, since reflectivity is inherently dependent on the background velocity, each updated velocity model should ideally be accompanied by a re-estimation of reflectivity. This mismatch between velocity and reflectivity (Valensi et al., 2017) can hinder convergence and reduce inversion accuracy. In some cases, re-estimating the reflectivity based on the updated velocity model may even increase the misfit function, thereby preventing convergence. Furthermore, inaccuracies in the velocity model lead to defocused imaging. The reflectivity is typically derived from stacked images based on small-offset data. However, as indicated by the demigration operator in Eq. (2), small-offset reflections exhibit minimal traveltime differences, which limits their sensitivity to background velocity variations. As a result, long-offset data are generally required to effectively update the velocity model. These observations underscore the importance of properly accounting for the coupling between reflectivity and velocity in reflection-based velocity inversion.

3. Reflection traveltime inversion based on cross-correlation time shift estimation with full gradient

To address the coupling between reflectivity and velocity, we introduce the reflectivity as an explicit variable into the objective function. The modified objective function is expressed as,

$$\begin{aligned} & \min_{m_s(\mathbf{x})} \mathcal{J}(m_s(\mathbf{x})) = \min_{m_s(\mathbf{x})} \ell(d_{\mathrm{obs}}(\mathbf{x}_r, t, \mathbf{x}_s), d_{\mathrm{cal}}(\mathbf{x}_r, t, \mathbf{x}_s)) \\ & \text{s.t. } d_{\mathrm{cal}}(\mathbf{x}_r, t, \mathbf{x}_s) = \mathbf{C}[\mathbf{B}(m_s(\mathbf{x}))R(m_s(\mathbf{x}))] \end{aligned}, \tag{5}$$

where the reflectivity $\mathbf{R} = R(m_s(\mathbf{x}))$ is now considered a function of the estimated background velocity model $m_s(\mathbf{x})$. Applying the chain rule, the total derivative of the objective function with respect to the background velocity is

$$\frac{\mathrm{d}\mathcal{J}}{\mathrm{d}m_s(\mathbf{x})} = \frac{\partial \mathcal{J}}{\partial m_s(\mathbf{x})} + \sum_{\mathbf{x}'} \frac{\partial \mathcal{J}}{\partial R(\mathbf{x}')} \frac{\partial R(\mathbf{x}')}{\partial m_s(\mathbf{x})}, \tag{6}$$

where the first term $\frac{\partial \mathcal{J}}{\partial m_s(\mathbf{x})} = \mathbf{C}\frac{\partial \mathbf{B}(m_s(\mathbf{x}))}{\mathrm{d}m_s(\mathbf{x})} R(m_s(\mathbf{x}))$ represents the data perturbation induced directly by perturbations in the background velocity. The second term captures the indirect effect via reflectivity: $\frac{\partial R(\mathbf{x}')}{\partial m_s(\mathbf{x})}$ is the sensitivity of the reflectivity to the background velocity, and $\frac{\partial \mathcal{J}}{\partial R(\mathbf{x}')} = \mathbf{CB}(m_s(\mathbf{x}))$ represents the effect of reflectivity perturbations on the data misfit.

In reflection traveltime inversion, the traveltime misfit function is defined as

$$\begin{aligned} \mathcal{J}(\mathbf{m}_s) &= \frac{1}{2} \| T(d_{\mathrm{obs}}(\mathbf{x}_r, t, \mathbf{x}_s)) - T(d_{\mathrm{cal}}(\mathbf{x}_r, t, \mathbf{x}_s)) \|^2 \\ &= \frac{1}{2} \sum_s \sum_r \Delta t^2(\mathbf{x}_r, \mathbf{x}_s), \end{aligned} \tag{7}$$

where $T(\cdot)$ denotes the traveltime picking operator. We adopt a cross-correlation-based method to estimate traveltime shift (Luo and Schuster, 1991; Wu et al., 2024).

3.1. Partial derivative of the objective function with respect to the background velocity model

The first term in Eq. (6) represents the partial derivative of the objective function with respect to the background velocity model:

$$\frac{\partial \mathcal{J}}{\partial \mathbf{m}_s} = \frac{\partial \Delta \mathbf{t}^{\mathrm{T}}}{\partial \mathbf{m}_s} \Delta \mathbf{t} = \sum_s \sum_r \frac{\partial \Delta t(\mathbf{x}_r, \mathbf{x}_s)}{\partial m_s(\mathbf{x})} \Delta t(\mathbf{x}_r, \mathbf{x}_s). \tag{8}$$

Combining Eq. (8) and Eqs. (A.4)–(A.6), we obtain the partial derivative of the objective function with respect to the background velocity:

$$\frac{\partial \mathcal{J}}{\partial \mathbf{m}_s} = \sum_s \sum_r \int - \frac{\dot{d}_{\mathrm{obs}}(\mathbf{x}_r, t + \Delta t, \mathbf{x}_s) \Delta t(\mathbf{x}_r, \mathbf{x}_s)}{\int \ddot{d}_{\mathrm{obs}}(\mathbf{x}_r, t + \Delta t, \mathbf{x}_s) d_{\mathrm{cal}}(\mathbf{x}_r, t, \mathbf{x}_s) \mathrm{d}t} \frac{\partial u_{\mathrm{cal}}(\mathbf{x}_r, t, \mathbf{x}_s)}{\partial m_s(\mathbf{x})} \mathrm{d}t, \tag{9}$$

where $\dot{d}_{\mathrm{obs}}$ and $\ddot{d}_{\mathrm{obs}}$ denote the first-order and second-order derivatives with respect to time, respectively.

According to the Fréchet derivative of the reflection wavefield with respect to the background velocity model (Eq. (B.16)), the gradient of the objective function can be represented using adjoint wavefields:

$$\frac{\partial \mathcal{J}}{\partial \mathbf{m}_{\mathrm{s}}} = \sum_{\mathrm{s}} \int -\ddot{u}_0(\mathbf{x},t,\mathbf{x}_{\mathrm{s}}) p_{\mathrm{s}}(\mathbf{x},t,\mathbf{x}_{\mathrm{r}}) - \ddot{u}_{\mathrm{s}}(\mathbf{x},t,\mathbf{x}_{\mathrm{s}}) p_{\mathrm{r}}(\mathbf{x},t,\mathbf{x}_{\mathrm{r}}) \mathrm{d}t, \tag{10a}$$

$$y(\mathbf{x}_{\mathrm{r}},t,\mathbf{x}_{\mathrm{s}}) = -\frac{\dot{d}_{\mathrm{obs}}(\mathbf{x}_{\mathrm{r}},t+\Delta t,\mathbf{x}_{\mathrm{s}})\Delta t(\mathbf{x}_{\mathrm{r}},\mathbf{x}_{\mathrm{s}})}{\int \ddot{d}_{\mathrm{obs}}(\mathbf{x}_{\mathrm{r}},t+\Delta t,\mathbf{x}_{\mathrm{s}}) d_{\mathrm{cal}}(\mathbf{x}_{\mathrm{r}},t,\mathbf{x}_{\mathrm{s}})\mathrm{d}t}, \tag{10b}$$

$$p_{\mathrm{s}}(\mathbf{x},t,\mathbf{x}_{\mathrm{r}}) = \sum_{\mathrm{r}} \int y(\mathbf{x}_{\mathrm{r}},t,\mathbf{x}_{\mathrm{s}}) * g_{\mathrm{s}}(\mathbf{x},t,\mathbf{x}_{\mathrm{r}}) \mathrm{d}t, \tag{10b}$$

$$p_{\mathrm{r}}(\mathbf{x},t,\mathbf{x}_{\mathrm{r}}) = \sum_{\mathrm{r}} \int y(\mathbf{x}_{\mathrm{r}},t,\mathbf{x}_{\mathrm{s}}) * g_0(\mathbf{x},t,\mathbf{x}_{\mathrm{r}}) \mathrm{d}t, \tag{10c}$$

where $\mathbf{y} \equiv y(\mathbf{x}_{\mathrm{r}},t,\mathbf{x}_{\mathrm{s}})$ is defined as the adjoint source, $\mathbf{p}_{\mathrm{r}} \equiv p_{\mathrm{r}}(\mathbf{x},t,\mathbf{x}_{\mathrm{r}})$ and $\mathbf{p}_{\mathrm{s}} \equiv p_{\mathrm{s}}(\mathbf{x},t,\mathbf{x}_{\mathrm{r}})$ denote the background and reflection adjoint wavefields, respectively.

3.2. Partial derivative of the objective function with respect to reflectivity

The second component of Eq. (6), the partial derivative of the objective function with respect to reflectivity, is given by,

$$\frac{\partial \mathcal{J}}{\partial \mathbf{R}} = \frac{\partial \Delta \mathbf{t}^{\mathrm{T}}}{\partial \mathbf{R}} \Delta \mathbf{t} = \sum_{\mathrm{s}} \sum_{\mathrm{r}} \frac{\partial \Delta t(\mathbf{x}_{\mathrm{r}},\mathbf{x}_{\mathrm{s}})}{\partial R(\mathbf{x})} \Delta t(\mathbf{x}_{\mathrm{r}},\mathbf{x}_{\mathrm{s}}). \tag{11}$$

Combining Eq. (11) and Eqs. (A.7)–(A.9), we can derive the expression for the partial derivative of the objective function with respect to reflectivity:

$$\frac{\partial \mathcal{J}}{\partial \mathbf{R}} = \sum_{\mathrm{s}} \sum_{\mathrm{r}} \int -\frac{\dot{d}_{\mathrm{obs}}(\mathbf{x}_{\mathrm{r}},t+\Delta t,\mathbf{x}_{\mathrm{s}})\Delta t(\mathbf{x}_{\mathrm{r}},\mathbf{x}_{\mathrm{s}})}{\int \ddot{d}_{\mathrm{obs}}(\mathbf{x}_{\mathrm{r}},t+\Delta t,\mathbf{x}_{\mathrm{s}}) d_{\mathrm{cal}}(\mathbf{x}_{\mathrm{r}},t,\mathbf{x}_{\mathrm{s}}) dt} \frac{\partial u_{\mathrm{cal}}(\mathbf{x}_{\mathrm{r}},t,\mathbf{x}_{\mathrm{s}})}{\partial R(\mathbf{x})} \mathrm{d}t. \tag{12}$$

According to the Fréchet derivative of the reflected wavefield with respect to reflectivity (Eq. (B.18)) and the adjoint source defined in Eq. (10b), the corresponding derivative of the objective function is:

$$\frac{\partial \mathcal{J}}{\partial \mathbf{R}} = \sum_{\mathrm{s}} \sum_{\mathrm{r}} \int y(\mathbf{x}_{\mathrm{r}},t,\mathbf{x}_{\mathrm{s}}) \left(-\ddot{u}_0(\mathbf{x},t,\mathbf{x}_{\mathrm{s}}) * g_0(\mathbf{x},t,\mathbf{x}_{\mathrm{r}}) \right) \mathrm{d}t. \tag{13}$$

Finally, based on the adjoint wavefield defined in Eq. (10c), the partial derivative of the objective function with respect to reflectivity can be written as,

$$\frac{\partial \mathcal{J}}{\partial \mathbf{R}} = \sum_{\mathrm{s}} \int -\ddot{u}_0(\mathbf{x},t,\mathbf{x}_{\mathrm{s}}) p_{\mathrm{r}}(\mathbf{x},t,\mathbf{x}_{\mathrm{r}}) \mathrm{d}t. \tag{14}$$

3.3. Partial derivative of reflectivity with respect to the background velocity model

We now consider the second part of the second term in Eq. (6): the perturbation of reflectivity induced by changes in the background velocity model. Based on the migration and demigration processes, we note that the traveltime of simulated and observed data are approximately invariant at zero or small offsets. Under this assumption, the reflectivity can be approximately represented within the current velocity model as:

$$R(\mathbf{x}) \approx \sum_{\mathrm{s}} W(\mathbf{x},\theta) \int u_0(\mathbf{x},t,\mathbf{x}_{\mathrm{s}}) u_{\mathrm{r}}(\mathbf{x},t,\mathbf{x}_{\mathrm{r}}) \mathrm{d}t, \tag{15a}$$

$$u_0(\mathbf{x},t,\mathbf{x}_{\mathrm{s}}) = f(t) * g_0(\mathbf{x},t,\mathbf{x}_{\mathrm{s}}), \tag{15b}$$

$$u_{\mathrm{r}}(\mathbf{x},t,\mathbf{x}_{\mathrm{r}}) = g_0(\mathbf{x},t,\mathbf{x}_{\mathrm{r}}) * d_{\mathrm{obs}}(\mathbf{x}_{\mathrm{r}},t,\mathbf{x}_{\mathrm{s}}), \tag{15c}$$

$$W(\mathbf{x},\theta) = \begin{cases} 1 & \theta < \theta_0 \\ 0 & \text{else} \end{cases}, \tag{15d}$$

where $u_0(\mathbf{x},t,\mathbf{x}_{\mathrm{s}})$ and $u_{\mathrm{r}}(\mathbf{x},t,\mathbf{x}_{\mathrm{r}})$ denote the source and receiver wavefields, respectively, propagated from the source $\mathbf{x}_{\mathrm{s}}$ and receiver $\mathbf{x}_{\mathrm{r}}$. θ is the local scattering angle between the two wavefields, and $W(\mathbf{x},\theta)$ is the angle-dependent weight function. θ_0 denotes a small-angle threshold coefficient. We compute the wavefield propagation angles using the Poynting vector method (Yoon and Marfurt, 2006; Yan and Dickens, 2016).

From Eq. (15a), the partial derivative of reflectivity with respect to the background velocity model can be expressed as:

$$\frac{\partial R(\mathbf{x}')}{\partial m_{\mathrm{s}}} = \sum_{\mathrm{s}} W(\mathbf{x},\theta) \int \left(\frac{\partial u_0(\mathbf{x}',t,\mathbf{x}_{\mathrm{s}})}{\partial m_{\mathrm{s}}(\mathbf{x})} u_{\mathrm{r}}(\mathbf{x}',t,\mathbf{x}_{\mathrm{r}}) + u_0(\mathbf{x}',t,\mathbf{x}_{\mathrm{s}}) \frac{\partial u_{\mathrm{r}}(\mathbf{x}',t,\mathbf{x}_{\mathrm{r}})}{\partial m_{\mathrm{s}}(\mathbf{x})} \right) \mathrm{d}t. \tag{16}$$

Based on Eqs. (B.11) and (B.12), and by combining Eqs. (14) and (16), we obtain

$$\frac{\partial \mathcal{J}}{\partial R(\mathbf{x}')} \frac{\partial R(\mathbf{x}')}{\partial m_{\mathrm{s}}(\mathbf{x}')} = \sum_{\mathrm{s}} \int W(\mathbf{x},\boldsymbol{\theta}) \begin{pmatrix} -\ddot{u}_0(\mathbf{x},t,\mathbf{x}_{\mathrm{s}}) & (-g_0(\mathbf{x},t,\mathbf{x}') * \ddot{u}_{\mathrm{r}}(\mathbf{x}',t,\mathbf{x}_{\mathrm{r}})) & (u_0(\mathbf{x}',t,\mathbf{x}_{\mathrm{s}}) p_{\mathrm{r}}(\mathbf{x}',t,\mathbf{x}_{\mathrm{r}})) \\ -\ddot{u}_{\mathrm{r}}(\mathbf{x},t,\mathbf{x}_{\mathrm{r}}) & (-g_0(\mathbf{x},t,\mathbf{x}') * \ddot{u}_0(\mathbf{x}',t,\mathbf{x}_{\mathrm{s}})) & (u_0(\mathbf{x}',t,\mathbf{x}_{\mathrm{s}}) p_{\mathrm{r}}(\mathbf{x}',t,\mathbf{x}_{\mathrm{r}})) \end{pmatrix} \mathrm{d}t. \tag{17}$$

To simplify notation, we define the following imaging condition:

$$\tilde{I}(\mathbf{x}) = u_0(\mathbf{x},t,\mathbf{x}_{\mathrm{s}}) p_{\mathrm{r}}(\mathbf{x},t,\mathbf{x}_{\mathrm{r}}). \tag{18}$$

Because $p_{\mathrm{r}}(\mathbf{x},t,\mathbf{x}_{\mathrm{r}})$ is the backward-propagated adjoint wavefield constructed from a traveltime-based adjoint source, we refer to Eq. (18) as the traveltime-mismatch imaging condition. Unlike conventional imaging conditions, which are formed by back-propagating observed seismic data and therefore persist regardless of velocity accuracy, the traveltime-mismatch imaging condition explicitly encodes traveltime residual information. Its amplitude and spatial distribution are directly controlled by the magnitude of the traveltime mismatch. As the background velocity model is progressively updated and the traveltime mismatch decreases, the corresponding imaging response weakens and ultimately vanishes once kinematic consistency is achieved.

Substituting Eqs. (17) and (18) into the second term of Eq. (6), we finally obtain:

$$\sum_{\mathbf{x}'}\frac{\partial \mathscr{J}}{\partial R(\mathbf{x}')}\frac{\partial R(\mathbf{x}')}{\partial m_{\mathrm{s}}(\mathbf{x})}=\sum_{\mathrm{s}}\int W(\mathbf{x},\boldsymbol{\theta})\big(-\ddot{u}_0(\mathbf{x},t,\mathbf{x}_{\mathrm{s}})q_{\mathrm{r}}(\mathbf{x},t,\mathbf{x}_{\mathrm{r}}) - \ddot{q}_{\mathrm{s}}(\mathbf{x},t,\mathbf{x}_{\mathrm{s}})u_{\mathrm{r}}(\mathbf{x},t,\mathbf{x}_{\mathrm{r}})\big)\mathrm{d}t, \tag{19a}$$

$$q_{\mathrm{r}}(\mathbf{x},t,\mathbf{x}_{\mathrm{r}})=\sum_{\mathbf{x}'}-g_0(\mathbf{x},t,\mathbf{x}')\tilde{I}(\mathbf{x}')*\ddot{u}_{\mathrm{r}}(\mathbf{x}',t,\mathbf{x}_{\mathrm{r}}), \tag{19b}$$

$$q_{\mathrm{s}}(\mathbf{x},t,\mathbf{x}_{\mathrm{s}})=\sum_{\mathbf{x}'}-g_0(\mathbf{x},t,\mathbf{x}')\tilde{I}(\mathbf{x}')*\ddot{u}_0(\mathbf{x}',t,\mathbf{x}_{\mathrm{s}}), \tag{19c}$$

where $q_{\mathrm{s}}(\mathbf{x},t,\mathbf{x}_{\mathrm{s}})$ represents the virtual reflected wavefield generated by the incident source wavefield $u_0^{\mathrm{s}}(\mathbf{x}',t,\mathbf{x}_{\mathrm{s}})$ at the image location $\tilde{I}(\mathbf{x}')$, and $q_{\mathrm{r}}(\mathbf{x},t,\mathbf{x}_{\mathrm{r}})$ corresponds to the reverse-time propagated virtual receiver wavefield $u_0^{\mathrm{r}}(\mathbf{x}',t,\mathbf{x}_{\mathrm{r}})$ reflected at the image $\tilde{I}(\mathbf{x}')$.

3.4. Total derivative of the objective function with respect to the background velocity model

Finally, by substituting Eq. (10a) and Eq. (19a) into the chain rule expression in Eq. (6), we obtain the total derivative of the objective function with respect to the background velocity model,

$$\mathbf{grad}=\frac{\mathrm{d}\mathscr{J}}{\mathrm{d}m_{\mathrm{s}}(\mathbf{x})}=\sum_{\mathrm{s}}\int -\ddot{u}_0(\mathbf{x},t,\mathbf{x}_{\mathrm{s}})p_{\mathrm{s}}(\mathbf{x},t,\mathbf{x}_{\mathrm{r}})-\ddot{u}_{\mathrm{s}}(\mathbf{x},t,\mathbf{x}_{\mathrm{s}})p_{\mathrm{r}}(\mathbf{x},t,\mathbf{x}_{\mathrm{r}})\mathrm{d}t+ \sum_{\mathrm{s}}\int W(\mathbf{x},\theta)\Big(-\ddot{u}_0(\mathbf{x},t,\mathbf{x}_{\mathrm{s}})q_{\mathrm{r}}(\mathbf{x},t,\mathbf{x}_{\mathrm{r}})-\ddot{q}_{\mathrm{s}}(\mathbf{x},t,\mathbf{x}_{\mathrm{s}})u_{\mathrm{r}}(\mathbf{x},t,\mathbf{x}_{\mathrm{r}})\Big)\mathrm{d}t. \tag{20}$$

The total derivative of the objective function with respect to the background velocity includes contributions from both explicit and implicit terms. We refer to this as the full gradient in the context of inversion.

We analyze the physical meaning of the gradient terms in Eq. (20). The first term represents the conventional gradient used in reflection traveltime inversion, which accounts for traveltime shifts caused by perturbations in the background velocity. Specifically, the first component of this term corresponds to the convolution between the second time derivative of the forward-propagated background source wavefield $\ddot{u}_0(\mathbf{x},t,\mathbf{x}_{\mathrm{s}})$ and the adjoint reflection wavefield $p_{\mathrm{s}}(\mathbf{x}, t,\mathbf{x}_{\mathrm{r}})$, which is generated by back-propagating the Green's function from the receiver location to the scattering point in the perturbed medium, as shown in Fig. 1(a). The second component involves the convolution between the forward-propagated reflection wavefield $\ddot{u}_{\mathrm{s}}(\mathbf{x}, t, \mathbf{x}_{\mathrm{s}})$, generated by velocity perturbations, and the adjoint background wavefield $p_{\mathrm{r}}(\mathbf{x},t,\mathbf{x}_{\mathrm{r}})$, back-propagated from the receiver side, as shown in Fig. 1(b). Together, these two contributions form the reflection tomography gradient, producing the characteristic "rabbit-ear" wave path pattern shown in Fig. 1(c).

The second term in Eq. (20) accounts for the coupling between reflectivity and velocity. If the reflectivity (i.e., the depth position of reflectors) is assumed to be independent of the background velocity, then the first term alone would suffice for updating the velocity model, and the partial derivative would be equivalent to the full derivative. However, in practice, the positions of subsurface reflectors are not known a priori—reflectivity is derived from migrated images, which themselves depend on the background velocity model. As a result, reflectivity and velocity are inherently coupled.

This coupling is captured by the second term of Eq. (20), which describes how perturbations in the background velocity affect the reflectivity and, consequently, the simulated reflection data. To better understand this, consider Eq. (19b) and Eq. (19c): the imaging condition generates the reflectors by correlating the background source wavefield with the adjoint wavefield (Eq. (18)). The presence of the adjoint wavefield—encoding the traveltime residual—is due to errors in both the background velocity and the reflector. These errors lead to traveltime shifts that are mapped into the new imaging result $\tilde{I}(\mathbf{x}')$. The forward-propagated background source wavefield $u_0(\mathbf{x}',t,\mathbf{x}_{\mathrm{s}})$ interacts with the imaging result $\tilde{I}(\mathbf{x}')$ (treated as a "secondary source") and produces a simulated reflection $q_{\mathrm{s}}(\mathbf{x}, t, \mathbf{x}_{\mathrm{s}})$. Similarly, the back-propagated receiver wavefield $u_{\mathrm{r}}(\mathbf{x}',t,\mathbf{x}_{\mathrm{r}})$ interacts with $\tilde{I}(\mathbf{x}')$ to generate an additional reflection contribution $q_{\mathrm{r}}(\mathbf{x}, t, \mathbf{x}_{\mathrm{r}})$. If both the background velocity and reflector depth are accurate—i.e., if there is no traveltime shift—the adjoint source becomes zero, and the imaging result $\tilde{I}(\mathbf{x}')$ vanishes. In this case, no secondary source exists, the reflection contributions $q_{\mathrm{s}}(\mathbf{x},t,\mathbf{x}_{\mathrm{s}})$ and $q_{\mathrm{r}}(\mathbf{x},t,\mathbf{x}_{\mathrm{r}})$ disappear, and the second gradient term becomes zero.

However, in practical scenarios where inaccuracies exist in either the velocity model or the reflector position, the adjoint wavefield remains nonzero, leading to a nonzero imaging result and associated reflection wave paths that can be used to update both the background velocity and the reflector structure. Notably, Eq. (20) restricts these wave paths to small-offset configurations. As shown in Fig. 1(d), one wave path is formed by the second time derivative of the background source wavefield $\ddot{u}_0(\mathbf{x},t,\mathbf{x}_{\mathrm{s}})$ from the source side and the simulated reflection wavefield $q_{\mathrm{r}}(\mathbf{x},t,\mathbf{x}_{\mathrm{r}})$. On the receiver side, another wave path is formed by the second derivative of the background wavefield $\ddot{u}_{\mathrm{r}}(\mathbf{x},t,\mathbf{x}_{\mathrm{r}})$ and the simulated reflection wavefield $q_{\mathrm{s}}(\mathbf{x}, t, \mathbf{x}_{\mathrm{s}})$, as shown in Fig. 1(e). These two wave paths overlap and interfere constructively, yielding the gradient shown in Fig. 1(f).

4. Reflection traveltime inversion using full gradient of characteristic reflection wavefield

Although the full-gradient reflection traveltime inversion derived in Section 3 provides a theoretically consistent framework

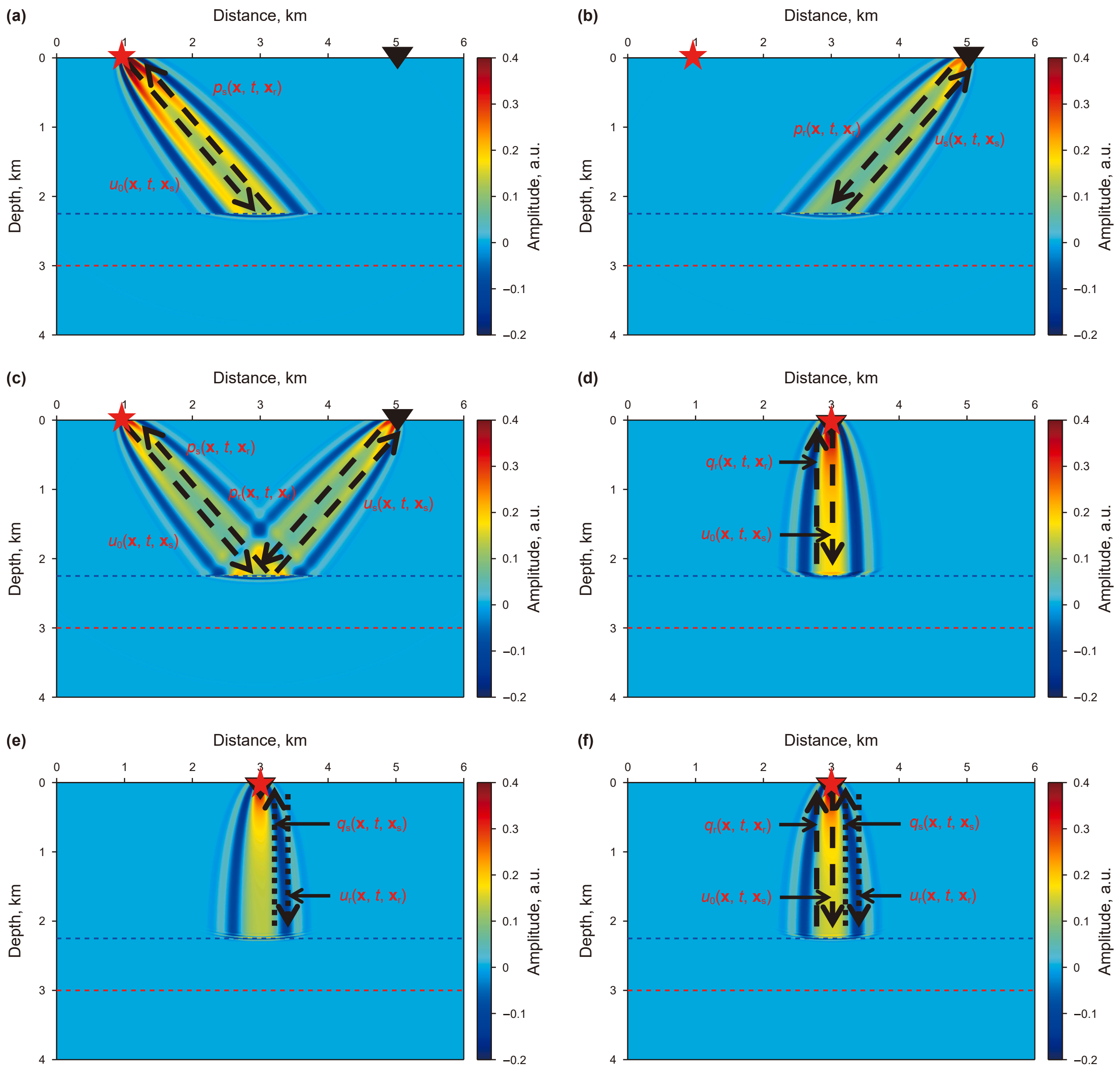

Fig. 1. Gradient responses from a single shot-receiver pair. **(a)** Partial result of the first term in Eq. (20); **(b)** another partial result of the first term; **(c)** sum of (a) and (b); **(d)** partial result of the second term in Eq. (20); **(e)** another partial result of the second term; **(f)** sum of (d) and (e). The shot and receiver positions are marked by red stars and black inverted triangles, respectively. Different wave paths are illustrated with black dashed lines.

for background velocity updating, its practical performance may be degraded by complex wave phenomena, noise, and interference among multiple reflection events in observed seismic data. Under such conditions, reliable traveltime shift estimation becomes challenging and may lead to unstable gradient updates.

To address this issue, we introduce characteristic reflection wavefields (CRWs) guided by characteristic reflector structures (CRSs). The central idea is to restrict the inversion to a subset of physically meaningful reflection events that dominantly control background velocity variations. By doing so, the robustness of traveltime measurements is improved, and the inversion process becomes more stable.

The proposed method builds upon the full-gradient formulation introduced in Section 3. Importantly, the mathematical structure of the full gradient remains unchanged. The introduction of CRSs affects only the construction of observed and simulated wavefields and the corresponding adjoint sources. Instead of using the entire reflection wavefield, the inversion is driven by CRWs associated with selected CRS horizons, which preserve the kinematic information relevant to background velocity updating while suppressing irrelevant or noisy wave components.

The overall workflow of the proposed CRS-guided full-gradient reflection traveltime inversion is summarized in Algorithm 1.

Algorithm 1
CRS-guided full-gradient reflection traveltime inversion.

Input:
Initial background velocity model $\mathbf{m}_0$
Observed seismic data $\mathbf{d}_{\text{obs}}$
Output:
Updated background velocity model $\mathbf{m}_s$
1. Perform prestack migration using the current background velocity model to generate common-image gathers (CIGs), stack the CIGs, and extract characteristic reflector structures (CRSs).
2. Demigrate the selected CRSs to obtain observed characteristic reflection wavefields (CRWs) $\mathbf{d}^{\text{c}}_{\text{obs}}$,
3. Generate simulated reflection wavefields using the extracted CRSs and the current background velocity model:
$$u^{\text{c}}_{\text{s}}(\mathbf{x}_{\text{r}},t,\mathbf{x}_{\text{s}}) = f(t)*g_0(\mathbf{x},t,\mathbf{x}_{\text{r}})*S(\mathbf{x}_{\text{s}}), \tag{21}$$
$$d^{\text{c}}_{\text{cal}}(\mathbf{x}_{\text{r}},t,\mathbf{x}_{\text{s}}) = \mathbf{C}\left[u^{\text{c}}_{\text{s}}(\mathbf{x}_{\text{r}},t,\mathbf{x}_{\text{s}})\right]. \tag{22}$$
4. Estimate traveltime shifts between observed and simulated CRWs using cross-correlation and construct the corresponding adjoint source:
$$y^{\text{c}}(\mathbf{x}_{\text{r}},t,\mathbf{x}_{\text{s}}) = -\frac{\dot{d}^{\text{c}}_{\text{obs}}(\mathbf{x}_{\text{r}},t+\Delta t,\mathbf{x}_{\text{s}})\Delta t(\mathbf{x}_{\text{r}},\mathbf{x}_{\text{s}})}{\int \ddot{d}^{\text{c}}_{\text{obs}}(\mathbf{x}_{\text{r}},t+\Delta t,\mathbf{x}_{\text{s}})d^{\text{c}}_{\text{cal}}(\mathbf{x}_{\text{r}},t,\mathbf{x}_{\text{s}})\text{d}t}. \tag{23}$$
5. Propagate the adjoint wavefields associated with CRWs and compute the corresponding adjoint-state variables.
6. Compute the full gradient of the objective function with respect to the background velocity model,
$$\begin{aligned}\mathbf{grad}^{\text{c}} &= \sum\nolimits_s \int -\ddot{u}_0(\mathbf{x},t,\mathbf{x}_{\text{s}})p^{\text{c}}_{\text{s}}(\mathbf{x},t,\mathbf{x}_{\text{r}}) - \ddot{u}^{\text{c}}_{\text{s}}(\mathbf{x},t,\mathbf{x}_{\text{s}})p^{\text{c}}_{\text{r}}(\mathbf{x},t,\mathbf{x}_{\text{r}})\text{d}t + \\ &\sum\nolimits_s \int W(\mathbf{x},\theta)\Big(-\ddot{u}_0(\mathbf{x},t,\mathbf{x}_{\text{s}})q^{\text{c}}_{\text{r}}(\mathbf{x},t,\mathbf{x}_{\text{r}}) - \ddot{q}^{\text{c}}_{\text{s}}(\mathbf{x},t,\mathbf{x}_{\text{s}})u^{\text{c}}_{\text{r}}(\mathbf{x},t,\mathbf{x}_{\text{r}})\Big)\text{d}t\end{aligned}. \tag{24}$$
7. Update the background velocity model using a gradient-based optimization scheme,
$$\mathbf{m}_{k+1} = \mathbf{m}_k - \alpha_k \text{P}(\mathbf{grad}^{\text{c}}_k). \tag{25}$$
where k denotes the iteration number, α_k is the step size, and P is a regularization operator.

Comparing Eq. (20) and Eq. (24), the primary difference lies in the definition of the adjoint source. In Eq. (20), the adjoint source is constructed directly from Eq. (10b), whereas in Eq. (24) it is defined by Eq. (23) based on characteristic reflection wavefields. Because the gradient accuracy strongly depends on the correctness of the adjoint source, this difference plays a critical role in the stability and effectiveness of the inversion.

In practical applications, seismic data often exhibit complex wave phenomena and various types of noise, which make accurate traveltime-shift estimation between observed and simulated data challenging. When the initial velocity model deviates significantly from the true model, the adjoint source defined by Eq. (10b) may become unreliable, leading to unstable or misleading gradient updates. To improve the robustness of traveltime estimation under such conditions, several approaches have been proposed, including time-lag FWI (Zhang et al., 2018; Wang et al., 2019, 2023; Vandrasi et al., 2020), enhanced template-matching FWI (Vigh et al., 2019; Kang et al., 2021; Cheng et al., 2023), and dynamic matching FWI (Mao et al., 2020; Huang et al., 2023).

In this study, we adopt the characteristic reflection wavefield (CRW) approach (Wu et al., 2024) to estimate traveltime shifts. Because CRWs contain only a limited number of well-defined and physically meaningful reflection events, the traveltime shifts associated with individual reflections can be measured more robustly. Consequently, the adjoint source defined in Eq. (23) is more accurate and less sensitive to noise and complex wave interference, ensuring that the resulting gradient is reliable and stable for velocity inversion. This improvement directly translates into more effective and consistent background velocity model updates.

Since CRS constraints enter the inversion exclusively through the construction of CRWs and their corresponding adjoint sources, the proposed method can be seamlessly integrated into existing wave-equation-based inversion frameworks. Moreover, the CRS-guided strategy provides a practical and physically motivated mechanism to stabilize full-gradient reflection traveltime inversion in the presence of noise and complex wave phenomena.

5. Experimental tests

To evaluate the effectiveness of the proposed full-gradient inversion method, we design a series of numerical experiments organized into four parts. First, a sensitivity analysis is conducted using a simple layered model to examine how the full-gradient formulation improves convergence behavior and resolution. Second, the method is applied to a more realistic and geologically complex modified two-dimensional overthrust model to assess its robustness. Third, a Marmousi model test is carried out to further demonstrate the capability of the proposed approach in recovering background velocity trends in a highly heterogeneous medium. Finally, a field data example is presented to validate the practical applicability of the method to real seismic data.

5.1. Sensitivity analysis of the full gradient

To validate the effectiveness of the full gradient, we use a series of numerical experiments with a layered velocity model. The true velocity model is shown in Fig. 2(a), where the reflector is located at a depth of 3 km. The first layer has a velocity of 2000 m/s, and the second layer has a velocity of 2500 m/s. The model spans 6 km laterally and 4 km in depth, with a uniform grid spacing of 10 m in both directions. Forward modeling is performed using a finite-difference scheme with 10th-order spatial and 2nd-order temporal accuracy. The source is a 25 Hz Ricker wavelet. The acquisition geometry consists of 151 evenly spaced shots between 0 and 6 km at 40 m intervals. For each shot, 1001 receivers are symmetrically deployed from −5000 m to 5000 m with a 10 m spacing. Seismic records are 6 s in duration with a 1 ms sampling interval. A single-shot record generated using the true velocity model, with the source located at 3 km, is shown in Fig. 3(a).

The background velocity model is a constant 1500 m/s, significantly lower than the true model. As a result, the migrated image is poorly focused. We extract zero-offset CIGs to generate the migration result shown in Fig. 2(b). In this figure, the red dashed line indicates the true reflector position, while the blue dashed line denotes the imaged reflector location. Using this image, simulated data are generated through a demigration process, as shown in Fig. 3(b). Fig. 3(a) and (b) compare the reflection traveltime positions derived from the true and demigrated records. The red dashed lines represent traveltimes from the true model, whereas the blue dashed lines correspond to the traveltimes from the demigrated data based on the background model. Fig. 3(c) shows the adjoint source computed using Eq. (10b).

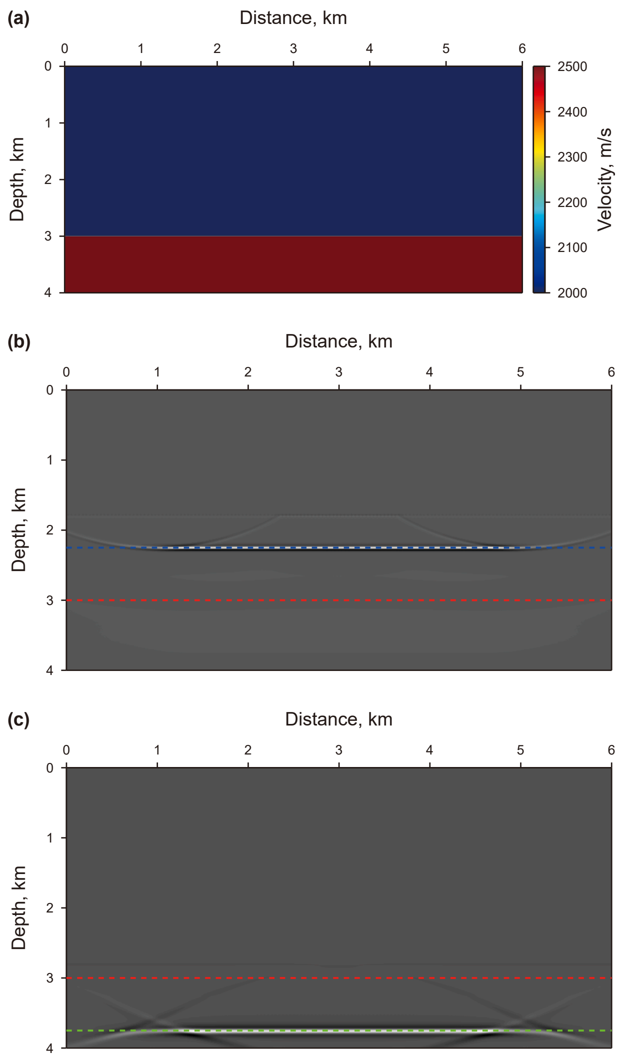

Fig. 2. **(a)** The true layered velocity model, where the first layer has a velocity of 2000 m/s and the second layer has a velocity of 2500 m/s, with a reflector located at 3 km depth; **(b)** migration result using a background constant velocity of 1500 m/s; **(c)** migration result using a background constant velocity of 2500 m/s. Red dashed lines indicate the true reflector position, blue dashed lines represent the imaged position using the 1500 m/s model, and green dashed lines represent the imaged position using the 2500 m/s model.

A comparison between the demigrated and true records reveals that for small (or zero) offsets, the traveltime differences are negligible due to the inherent time-invariance of the migration-demigration process. Consequently, reliable velocity updates cannot be obtained from small-offset data and must instead rely on large-offset information, as illustrated in Fig. 3(c). According to the demigration formulation (Eq. (B.4)), the process primarily utilizes focused energy from zero-offset or small-offset gathers. This explains the widespread use of small-offset data in seismic imaging. In practice, defocused energy is generally attenuated through multi-fold acquisition, which favors more coherent imaging results.

Fig. 4 shows the single-shot gradient results for a source located at 3 km. Fig. 4(a) shows the conventional gradient, corresponding to the first term in Eq. (20), while Fig. 4(b) shows the reflectivity-velocity coupling component, represented by the second term of Eq. (20). Fig. 4(c) shows the conventional gradient assuming the true reflector depths are known. Fig. 4(d) shows the full gradient, which combines both terms. A comparison of these results reveals that in Fig. 4(a), the gradient is absent at small offsets where the area is highlighted by red circle, indicating limited sensitivity in this region. In contrast, the full-gradient result in Fig. 4(d) successfully recovers the missing sensitivity, particularly at small offsets. Furthermore, the update directions in Fig. 4(a) and (b) are consistent, confirming that both terms in Eq. (20) contribute constructively to velocity updating. The multi-shot gradient, obtained by stacking 151 shots, is shown in Fig. 5. Fig. 5(a) and (b) show the first and second gradient terms, respectively. The similarity in update directions between these terms demonstrates the stability and robustness of the full-gradient formulation.

Figs. 6 and 7 show the single-shot and multi-shot gradient results, respectively, using an overestimated constant velocity model of 2500 m/s. Compared to the underestimated velocity model case, the gradient directions are reversed, which is consistent with physical intuition. This further validates the effectiveness of Eq. (20) in guiding velocity updates. Specifically, when the velocity is underestimated, the imaged reflectors appear shallower than their true positions (as shown by the blue dashed line in Fig. 2(b)), and the resulting negative gradient encourages deeper velocity updates. Conversely, when the velocity is overestimated, the reflectors appear too deep (as indicated by the green dashed line in Fig. 2(c)), and the gradient promotes upward corrections. When the velocity model is accurate, the reflector aligns with its true depth, and the second gradient term naturally vanishes.

We further assess the impact of the full gradient on inversion convergence. To isolate the influence of the gradient, we perform fixed-step-size iterative updates using both the conventional and full-gradient approaches. The initial velocity model is a constant 1500 m/s. All other parameters and the acquisition configuration are kept consistent with those in Fig. 5. Inversion results at different iteration steps are shown in Figs. 8 and 9. The results demonstrate that the full-gradient method achieves faster convergence and produces smoother, more geologically plausible velocity models.

Figs. 10 and 11 show comparisons of vertical profiles at different iterations. The full-gradient method produces results that are closer to the true velocity model and better capture the layered structure, further confirming the validity of the proposed approach. The convergence curves are plotted in Fig. 12, where the blue curve represents the conventional method and the red curve corresponds to the full-gradient method. The full-gradient method achieves convergence more than twice as fast as the conventional method. In terms of computational cost, partial wavefield components in Eq. (20) and Eq. (24) can be reused, improving overall efficiency. With a shot-parallel implementation, the computational overhead of the full-gradient method is approximately 1.75 times that of the conventional method. This overhead can be further reduced with optimized implementation strategies. Nevertheless, the benefits of significantly faster convergence and improved inversion accuracy justify the additional computational effort.

5.2. Modified 2D overthrust model test

To further assess the effectiveness of the proposed full-gradient inversion method, we apply it to a modified version of the 2D overthrust model. The true velocity model, shown in Fig. 13(a), spans 20 km laterally and 5.5 km in depth, with uniform grid spacing of 25 m in both directions. Wavefield modeling is

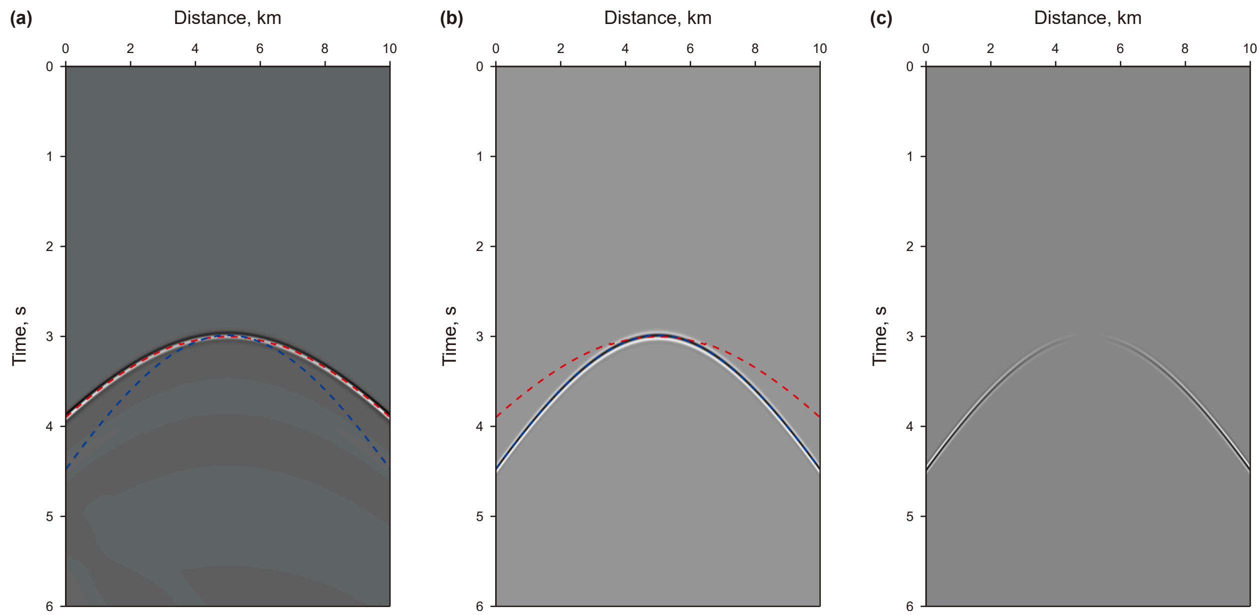

Fig. 3. **(a)** Single-shot seismic record simulated with the true velocity model; **(b)** demigrated single-shot record using the background velocity model (1500 m/s); **(c)** the corresponding adjoint source. Red dashed lines show reflection traveltimes computed from the true model, and blue dashed lines indicate those computed from the demigrated data using the background model.

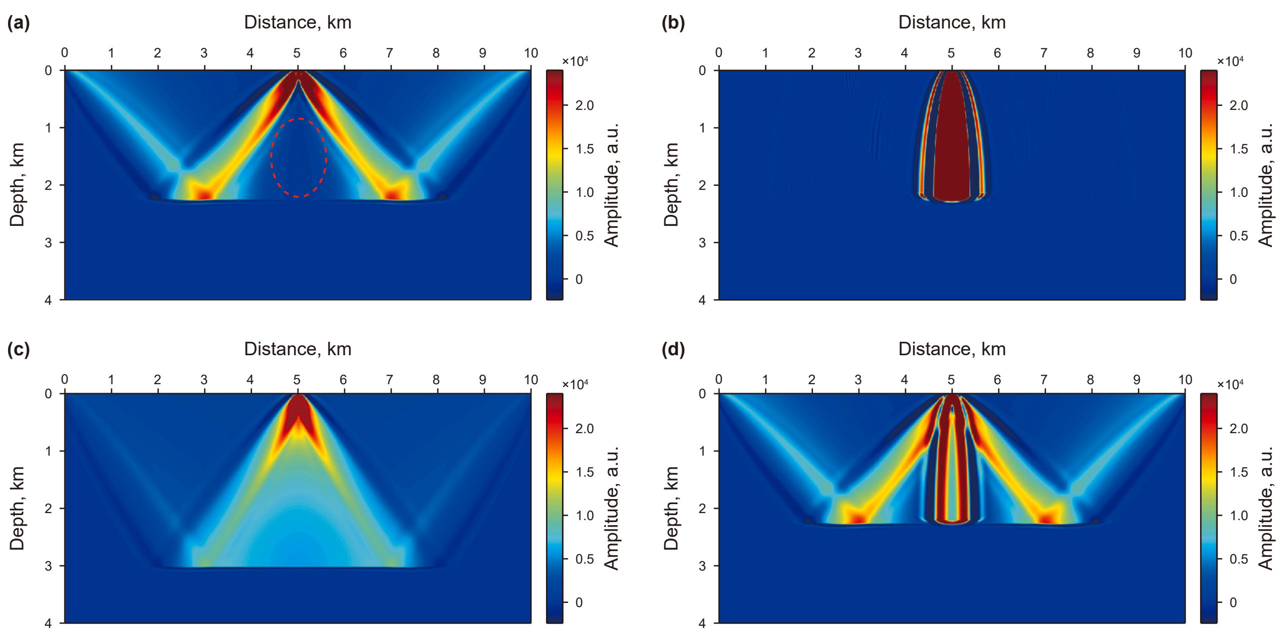

Fig. 4. Single-shot gradient results with the background velocity (1500 m/s). **(a)** Conventional gradient (first term of Eq. (20)); **(b)** reflectivity-velocity coupling term (second term of Eq. (20)); **(c)** conventional gradient assuming the true reflector depth is known; **(d)** full-gradient combining both terms.

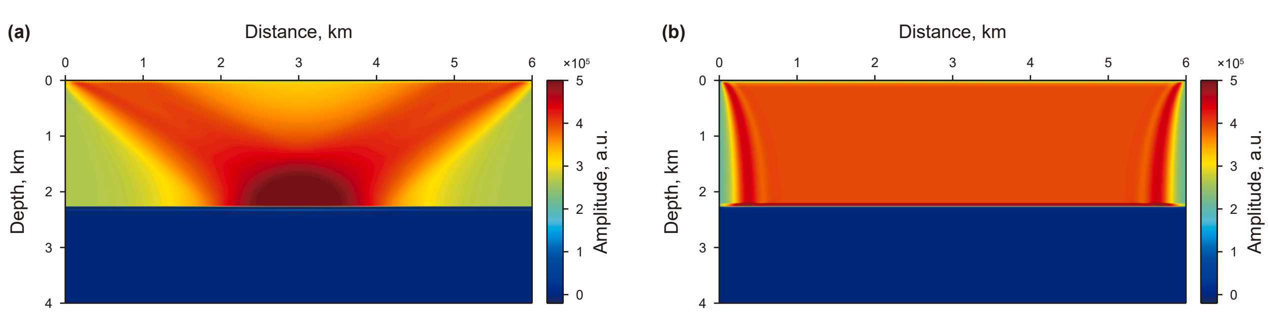

Fig. 5. Multi-shot gradient results with the background velocity (1500 m/s). **(a)** Conventional gradient (first term of Eq. (20)); **(b)** reflectivity-velocity coupling term (second term of Eq. (20)).

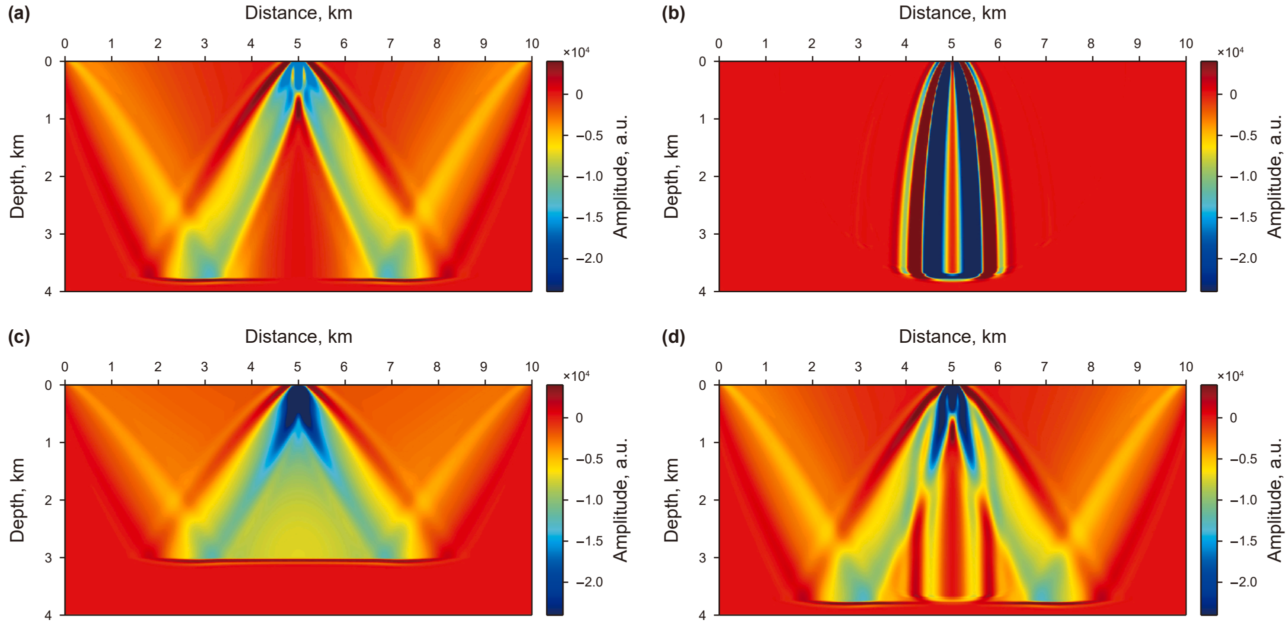

Fig. 6. Single-shot gradient results with the background velocity (2500 m/s). **(a)** Conventional gradient (first term of Eq. (20)); **(b)** reflectivity-velocity coupling term (second term of Eq. (20)); **(c)** conventional gradient assuming the true reflector depth is known; **(d)** full-gradient combining both terms.

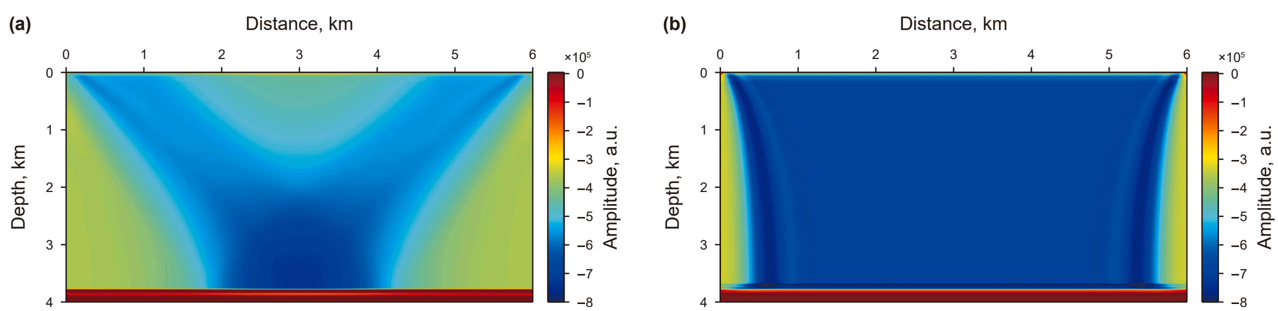

Fig. 7. Multi-shot gradient results with the background velocity (2500 m/s). **(a)** Conventional gradient (first term of Eq. (20)); **(b)** reflectivity-velocity coupling term (second term of Eq. (20)).

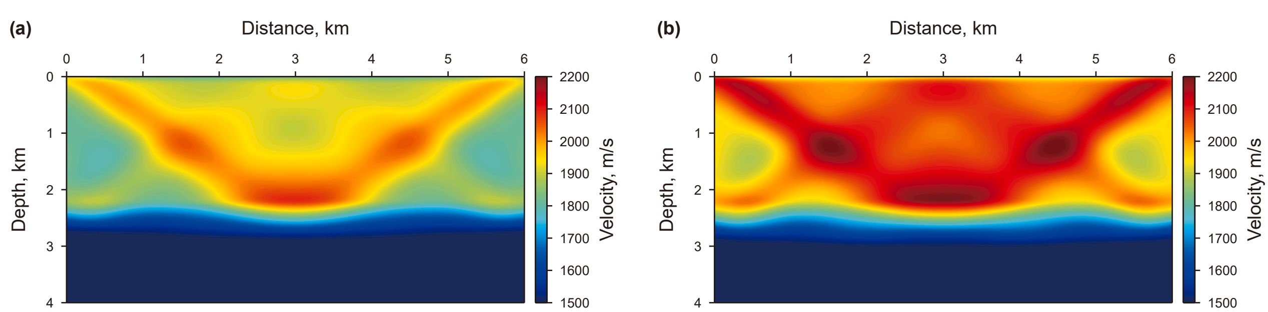

Fig. 8. Inversion results using the conventional gradient method at **(a)** iteration 15; **(b)** iteration 30.

performed using a 10th-order finite-difference scheme in space and a 2nd-order scheme in time. A 10 Hz Ricker wavelet is used as the source. A total of 401 shots are evenly distributed along the surface from 0 km to 20 km at 50 m intervals. Each shot is recorded by 401 receivers spaced at 25 m, covering offsets from −5 km to 5 km. The initial velocity model consists of a laterally homogeneous profile with a vertical velocity gradient, starting at 2178.83 m/s and increasing by 0.5 m/s per meter of depth. This initial model is shown in Fig. 13(b).

The observed CRW is extracted using Eq. (21), and the complete processing workflow is shown in Fig. 14. As shown in Fig. 14(a), the input seismic data are first migrated using prestack depth migration (PSDM) to generate CIGs, shown in Fig. 14(b). These gathers are then flattened and stacked using the method of Wu et al. (2025), and the characteristic reflector structure is extracted via the approach proposed in Wu et al. (2023a), as shown in Fig. 14(c). This structure is subsequently used to constrain the generation of characteristic CIGs (Wu et al., 2023b), which are demigrated to

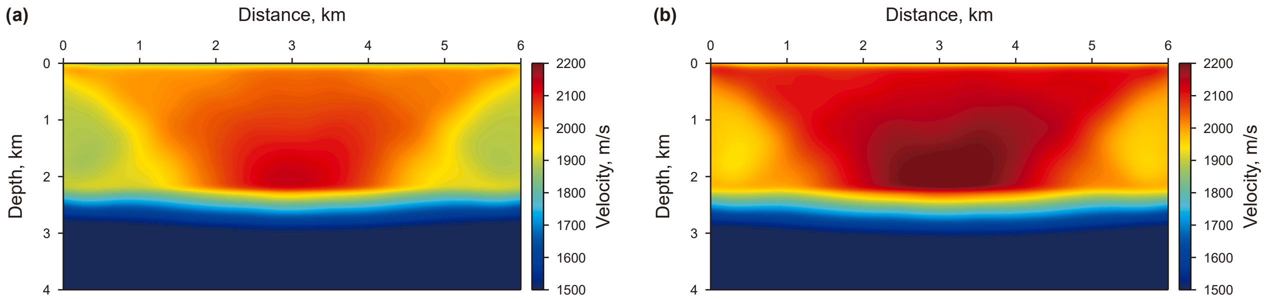

Fig. 9. Inversion results using the full-gradient method at **(a)** iteration 10; **(b)** iteration 15.

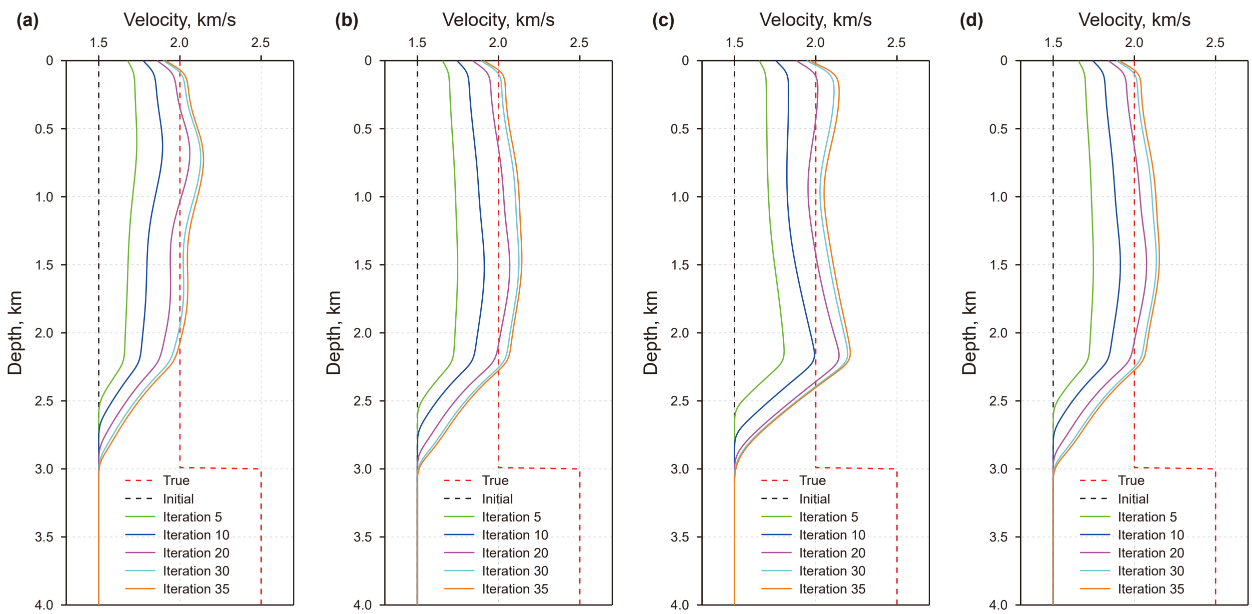

Fig. 10. Vertical profile comparisons using the conventional gradient method at surface locations: **(a)** 1.0 km; **(b)** 2.0 km; **(c)** 3.0 km; **(d)** 4.0 km. Dashed black lines: initial velocity; dashed red lines: true velocity; colored lines (green, blue, magenta, cyan, brown): inversion results after 5, 10, 20, 30, and 35 iterations.

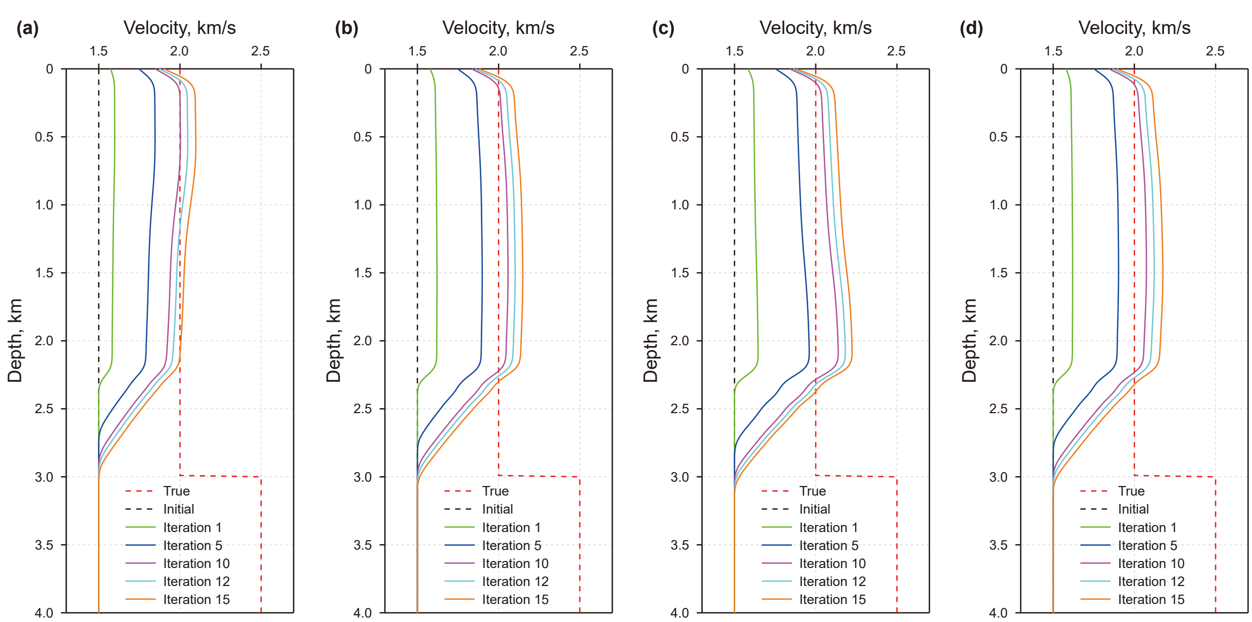

Fig. 11. Vertical profile comparisons using the full-gradient method at surface locations: **(a)** 1.0 km; **(b)** 2.0 km; **(c)** 3.0 km; **(d)** 4.0 km. Dashed black lines: initial velocity; dashed red lines: true velocity; colored lines (green, blue, magenta, cyan, brown): inversion results after 1, 5, 10, 12, and 15 iterations.

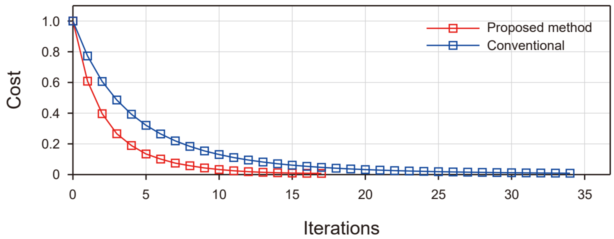

Fig. 12. Convergence curves comparison. Blue line: conventional gradient method; red line: proposed full-gradient method.

produce the observed CRW dataset (Wu et al., 2024), shown in Fig. 14(d).

We then assess the influence of the proposed full-gradient method on velocity model updating. Fig. 15(a) shows the inverted velocity model after 40 iterations using the conventional gradient-based inversion with CRWs, while Fig. 15(b) shows the result after only 20 iterations using the proposed full-gradient method. Notably, under the initial velocity model (Fig. 13(b)), conventional reflection traveltime inversion using the observed data (Fig. 14(a)) fails to converge when the traveltime differences are measured using the dynamic time

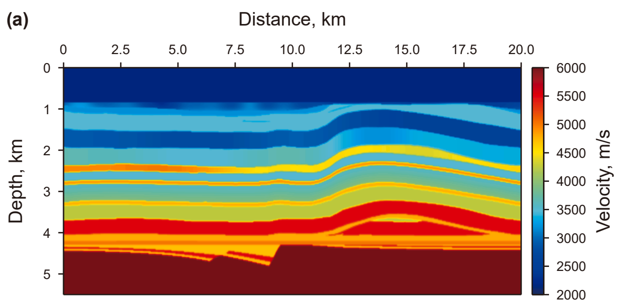

Fig. 13. Overthrust 2D velocity model. **(a)** True velocity model; **(b)** initial velocity model.

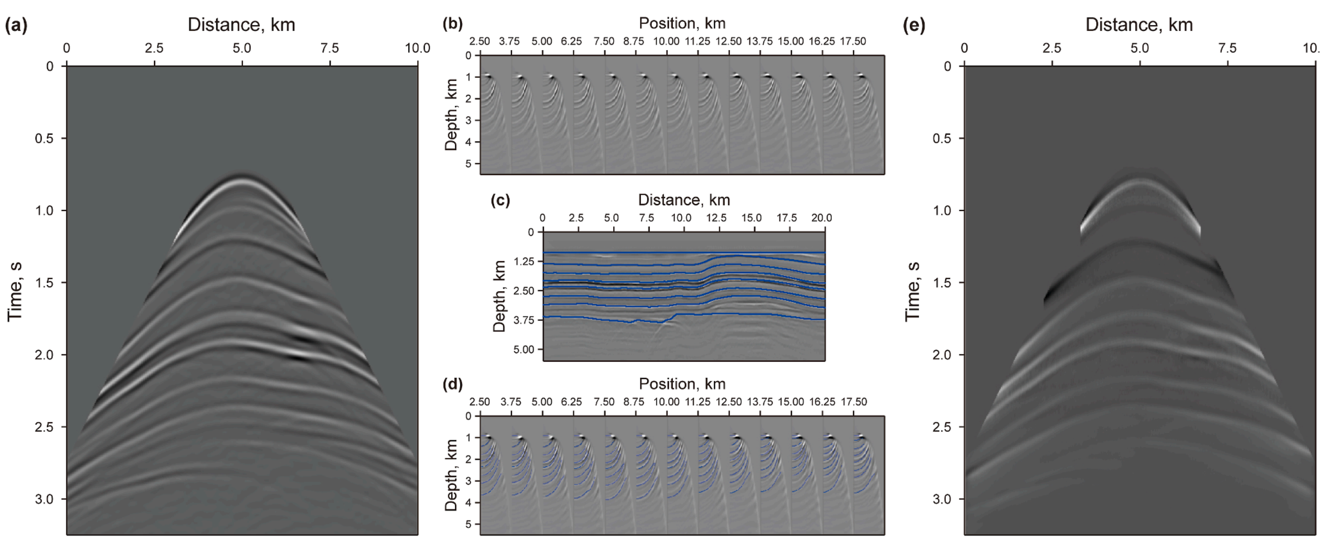

Fig. 14. Workflow for extracting observed characteristic reflection wavefields (CRWs). **(a)** Raw observed seismic data; **(b)** common image gathers (CIGs) using the initial model; **(c)** characteristic reflector structure; **(d)** characteristic CIGs; **(e)** observed CRWs generated based on CRS constraints.

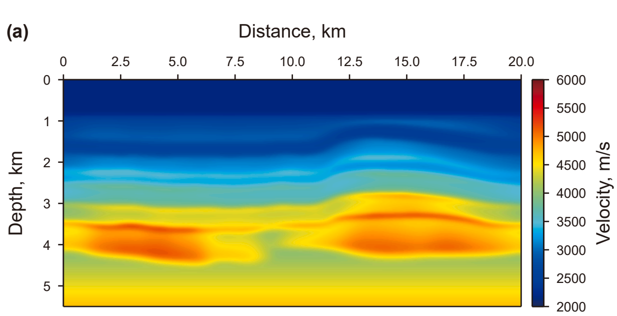

Fig. 15. Inverted velocity models using CRWs. **(a)** Conventional gradient method; **(b)** proposed full-gradient method.

warping (DTW) method. Therefore, we compare only the CRW-based inversions using the conventional gradient and the proposed full-gradient method. Both inversion strategies use identical parameters and a fixed step size to ensure a fair comparison. The results demonstrate that the proposed full-gradient method achieves more accurate reconstruction of the true subsurface velocity, with smoother and geologically more plausible structures. Figs. 16 and 17 show comparisons of vertical and horizontal velocity profiles, respectively. In both figures, the black line represents the initial model, the blue line represents the true model, and the red and green lines represent the results of the conventional and full-gradient methods, respectively. The results clearly indicate that the proposed method provides higher inversion accuracy and better recovery of the low-wavenumber velocity background trend.

To further validate the inversion quality, we perform PSDM using different velocity models. Fig. 18(a) shows the migration result using the initial model, while Fig. 18(b) and (c) show results using the models obtained from conventional and full-gradient inversions, respectively. As seen in Fig. 18(a), the initial model produces poor imaging quality with significant reflector depth errors and defocused reflectors. After conventional gradient inversion with CRWs, the reflector positions are improved and the image becomes more focused (Fig. 18(b)), but some areas remain inadequately imaged. By contrast, the migration result using the velocity model obtained from the proposed full-gradient method (Fig. 18(c)) shows reflectors

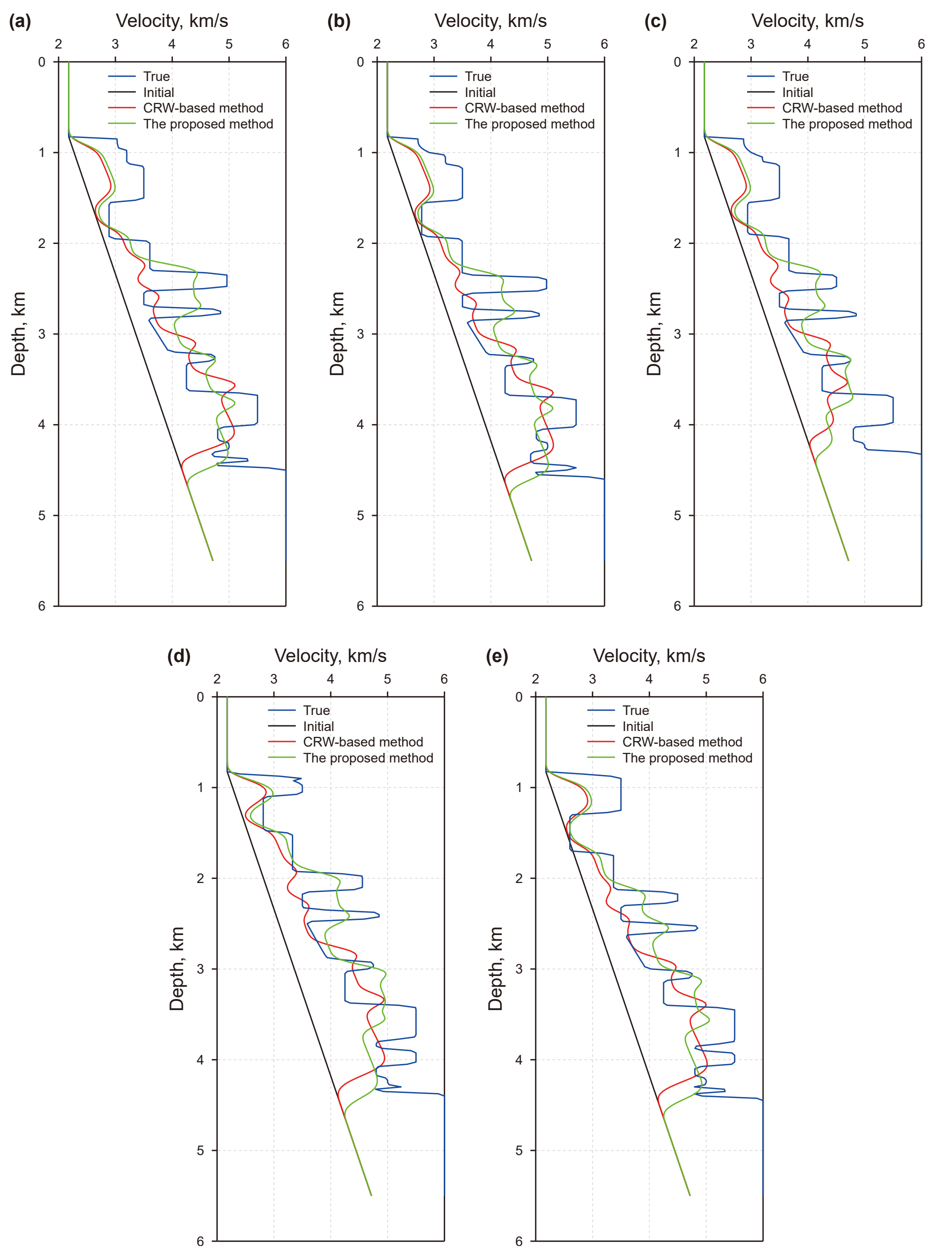

Fig. 16. Vertical profile comparisons at surface locations: **(a)** 2.5 km; **(b)** 5.0 km; **(c)** 10 km; **(d)** 12.5 km; **(e)** 17.5 km. Black lines: initial model; blue lines: true velocity; red and green lines: results from the conventional and full-gradient methods, respectively.

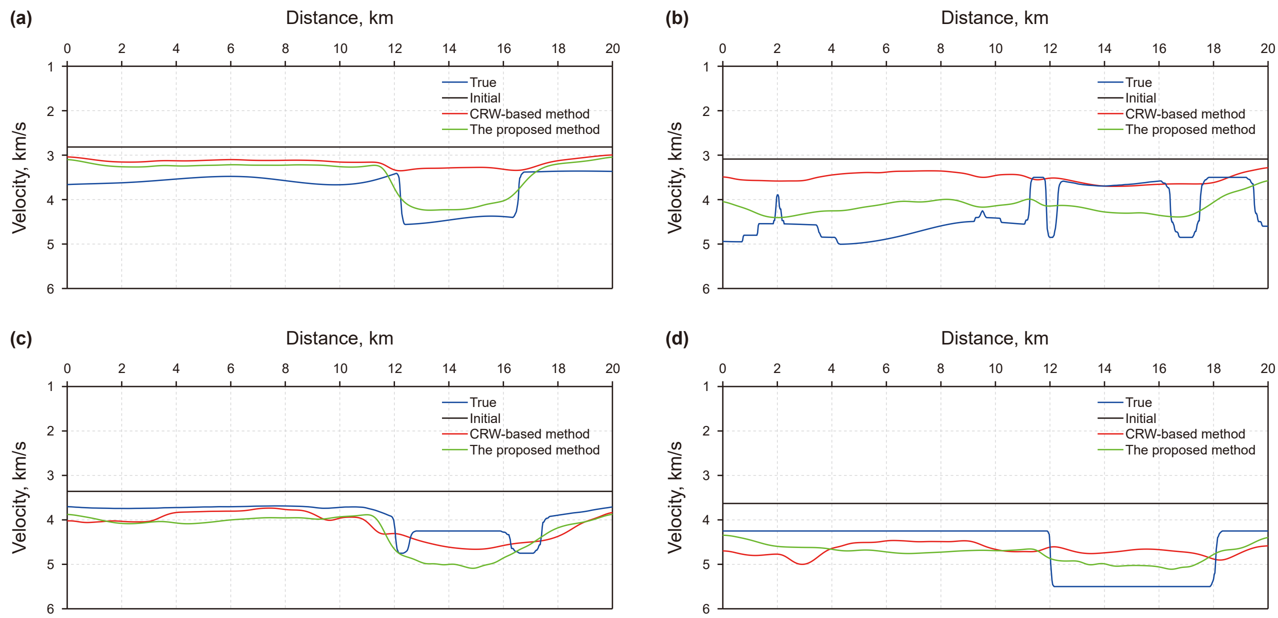

Fig. 17. Horizontal profile comparisons at depth locations: **(a)** 2.0 km; **(b)** 2.5 km; **(c)** 3.0 km; **(d)** 3.5 km. Black lines: initial model; blue lines: true velocity; red and green lines: results from the conventional and full-gradient methods, respectively.

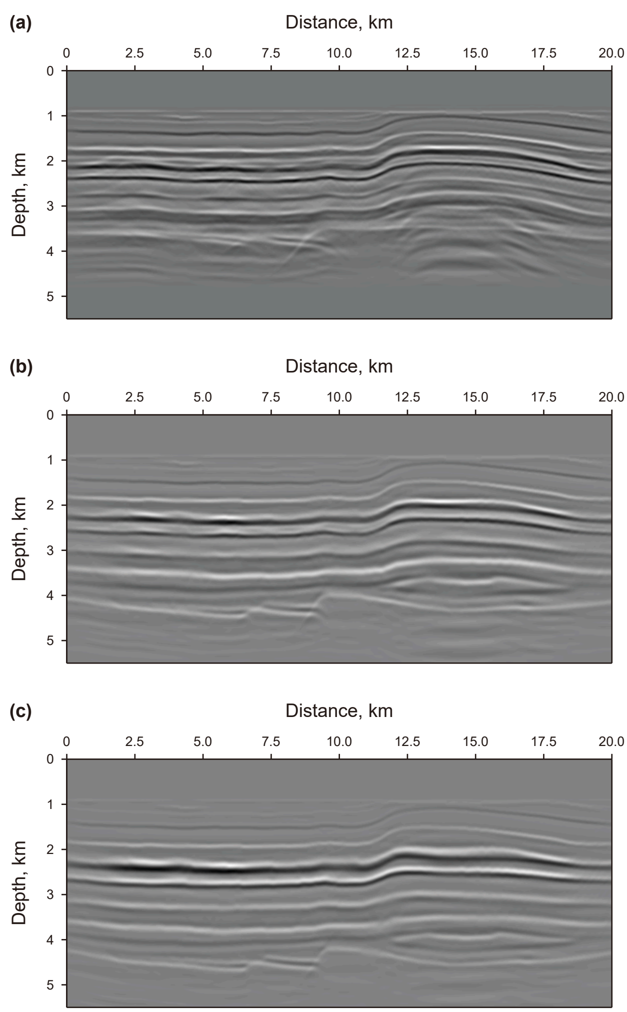

Fig. 18. Migration results using different velocity models. **(a)** Initial model; **(b)** inverted model using the conventional method; **(c)** inverted model using the proposed full-gradient method.

that align well with those in the true model, with better focusing and higher resolution. Fig. 19 shows CIGs migrated using different velocity models. While both the conventional and full-gradient methods improve event flattening, the gathers derived from the full-gradient inversion (Fig. 19(c)) are noticeably more coherent and horizontal, indicating more accurate velocity updates. These results demonstrate that the proposed full-gradient method significantly enhances both convergence speed and inversion accuracy.

5.3. *Marmousi model test*

We employ the Marmousi model to further demonstrate the velocity updating capability of the proposed method. The true velocity model is shown in Fig. 20(a), with a depth extent of 3.5 km and a lateral extent of 17 km, sampled at 10 m in both directions. The upper 0.5 km is a constant-velocity water layer with a velocity of 1500 m/s. To emphasize the ability of the proposed method to update the background velocity, we choose an initial model that significantly deviates from the true model: below 0.5 km depth, the velocity starts at 1500 m/s and increases linearly at a rate of 0.167 m/s per meter of depth, as shown in Fig. 20(b).

For the data acquisition setup, sources are uniformly distributed from 0 to 17 km with a shot interval of 100 m, resulting in a total of 171 shots. For each shot, receivers cover an offset range of −1.5 km to 1.5 km. A 10-Hz Ricker wavelet is used as the source, and the recording time is 4 s with a sampling interval of 0.5 ms. The observed data are preprocessed only by removing direct waves, without any additional processing. The processed data are shown in Fig. 21 where the source position is at 5 km.

The inversion is carried out in three stages. In the first two stages, we apply the proposed CRW based full gradient reflection wave-equation traveltime inversion, while in the third stage, conventional FWI is used. In the first stage, three characteristic reflection structures are selected, and in the second stage, six characteristic reflection structures are used. The step length is gradually reduced over the three stages.

Prestack Kirchhoff depth migration is first performed using the initial velocity model, and the small-angle stacked image is shown

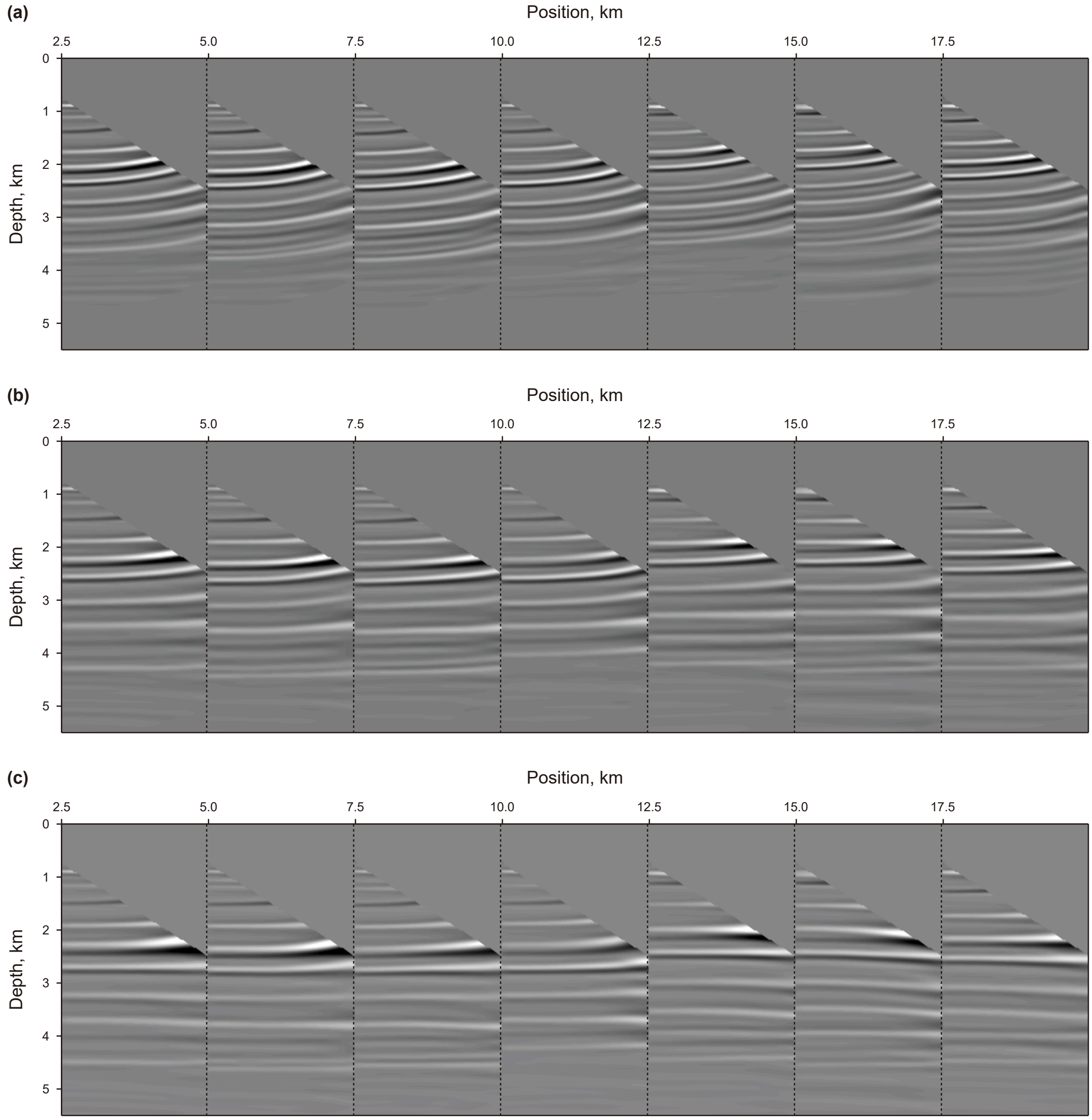

Fig. 19. CIGs generated using (**a**) the initial model; (**b**) the inverted model from the conventional method; (**c**) the inverted model from the proposed full-gradient method. The CIGs are extracted at every 2.5 km, with an offset range of 0–5 km and 25 m spacing.

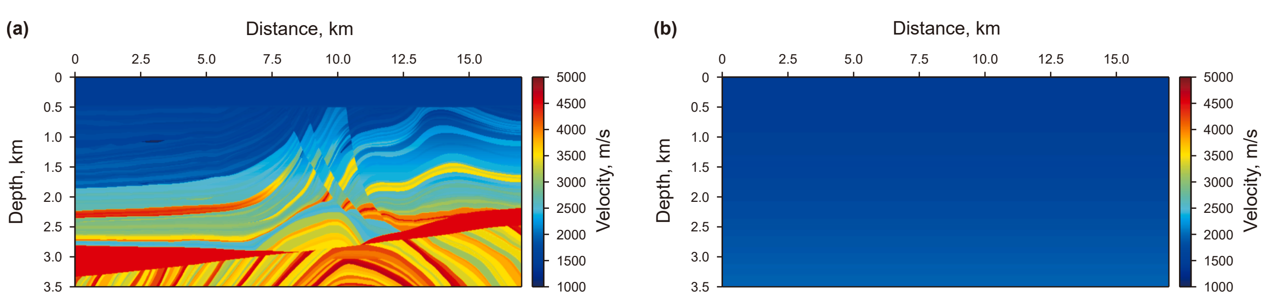

Fig. 20. The Marmousi velocity model. (**a**) True velocity model; (**b**) initial velocity model.

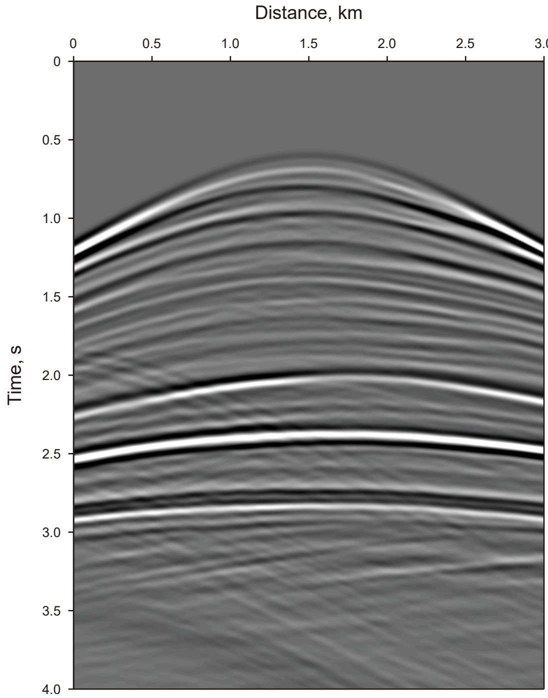

Fig. 21. Common-shot gather after direct-wave removal (source location at 5 km).

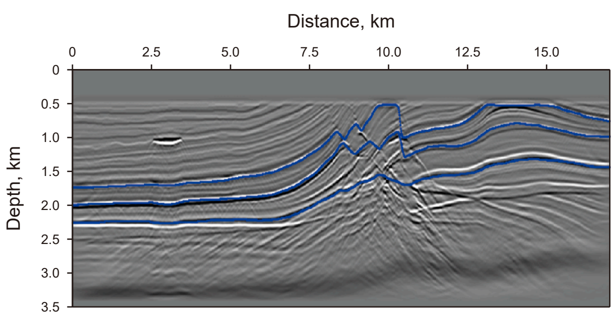

Fig. 22. Migration result obtained using the initial velocity model where the green lines denote the selected characteristic reflection horizons.

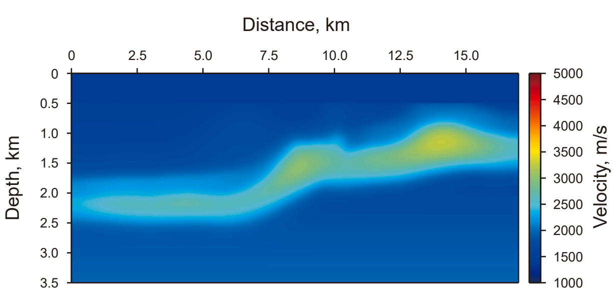

Fig. 23. Velocity model after the first-stage inversion.

in Fig. 22. Due to the large discrepancy between the initial and true velocity models, the migration quality is poor; therefore, only clearly identifiable reflectors are selected for inversion (blue lines in Fig. 22). After five iterations, the updated velocity model is shown in Fig. 23, where noticeable updates are observed in parts of

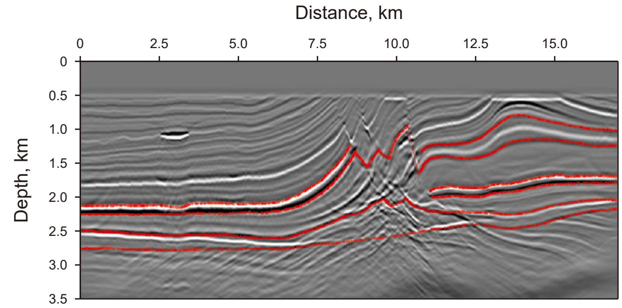

Fig. 24. Migration result obtained using the velocity model from the first-stage inversion where the red lines denote the selected characteristic reflection horizons.

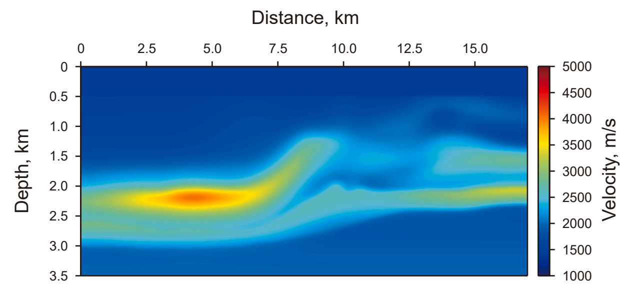

Fig. 25. Velocity model after the second-stage inversion.

the model. Migration using this updated model (Fig. 24) shows that reflector positions are better aligned and reflection events become clearer compared to Fig. 22. Based on this improved image, additional characteristic reflectors are selected (red lines in Fig. 24), and ten further iterations are performed. The resulting velocity model (Fig. 25) shows a clear improvement in the background velocity trend and matches the true model in Fig. 20(a) much more closely.

To further assess the inversion results, the CIGs corresponding to the initial and inverted velocity models are extracted and compared (Fig. 26). The CIGs associated with the initial velocity model exhibit strong curvature and non-flat events, while those obtained after inversion are largely flattened and correctly positioned in depth. The stacked images derived from these CIGs are shown in Fig. 27, demonstrating a significant improvement in imaging quality compared to Fig. 22.

Finally, the inverted velocity model is used as the initial model for FWI. After 100 iterations, the FWI-updated velocity model is shown in Fig. 28. The velocity above 3 km depth is well recovered and closely matches the true model, owing to the prior updates guided by characteristic reflection structures. Below 3 km depth, where no characteristic reflectors were selected, the velocity remains less accurate even after FWI iterations. This result highlights the importance of characteristic-structure selection: FWI can effectively refine the velocity model only when the background trend is sufficiently accurate.

A comparison of vertical velocity profiles extracted from the true, initial, and inverted models is also shown in Fig. 29. The blue curve represents the initial model, the black curve the true model, the green and cyan curves the results after the first and second stages of reflection traveltime inversion, respectively, and the red curve the final FWI result. The first-stage inversion updates the velocity trend but introduces local overcorrections due to the use of a relatively large step length. These anomalies are effectively

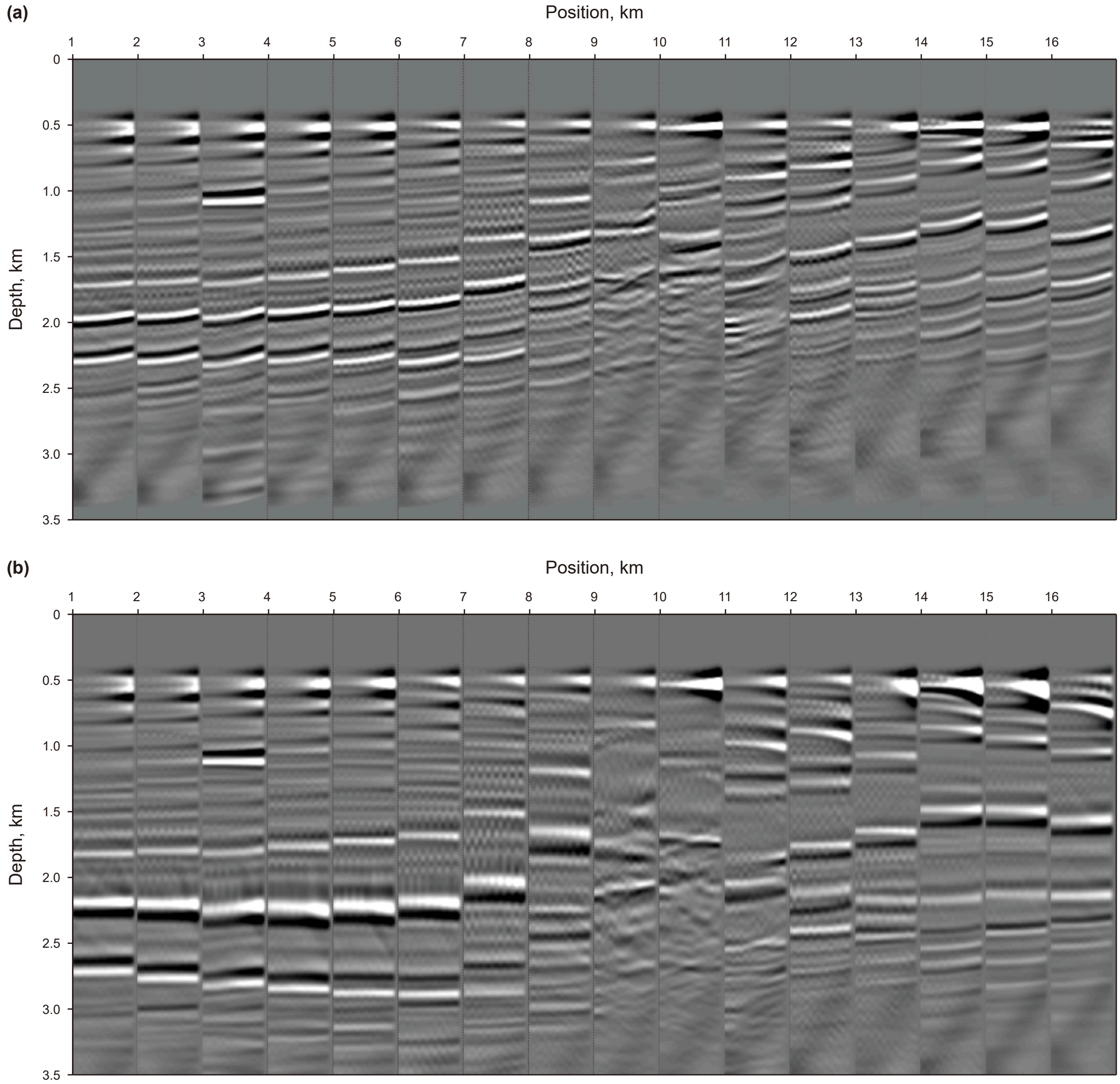

Fig. 26. CIGs generated using **(a)** the initial model; **(b)** the inverted model after the second-stage inversion. The CIGs are extracted at every 1.0 km, with an offset range of 0–800 m and 10 m spacing.

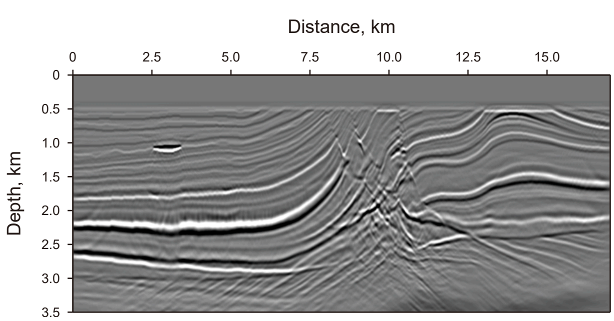

Fig. 27. Migration result obtained using the inverted model after the second-stage inversion.

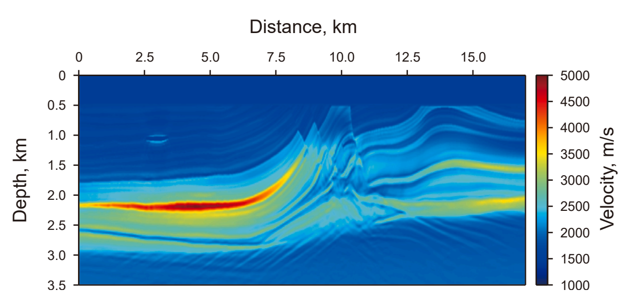

Fig. 28. Velocity model after full waveform inversion.

corrected in the second stage, leading to a more stable and geologically consistent background velocity model. Subsequent FWI further refines the model and yields a high-accuracy velocity estimate. These results demonstrate that the proposed method provides a reliable low-wavenumber background velocity foundation, which is essential for enabling successful and stable FWI updates in complex media; without such a background trend, FWI alone fails to recover deep velocity structures.

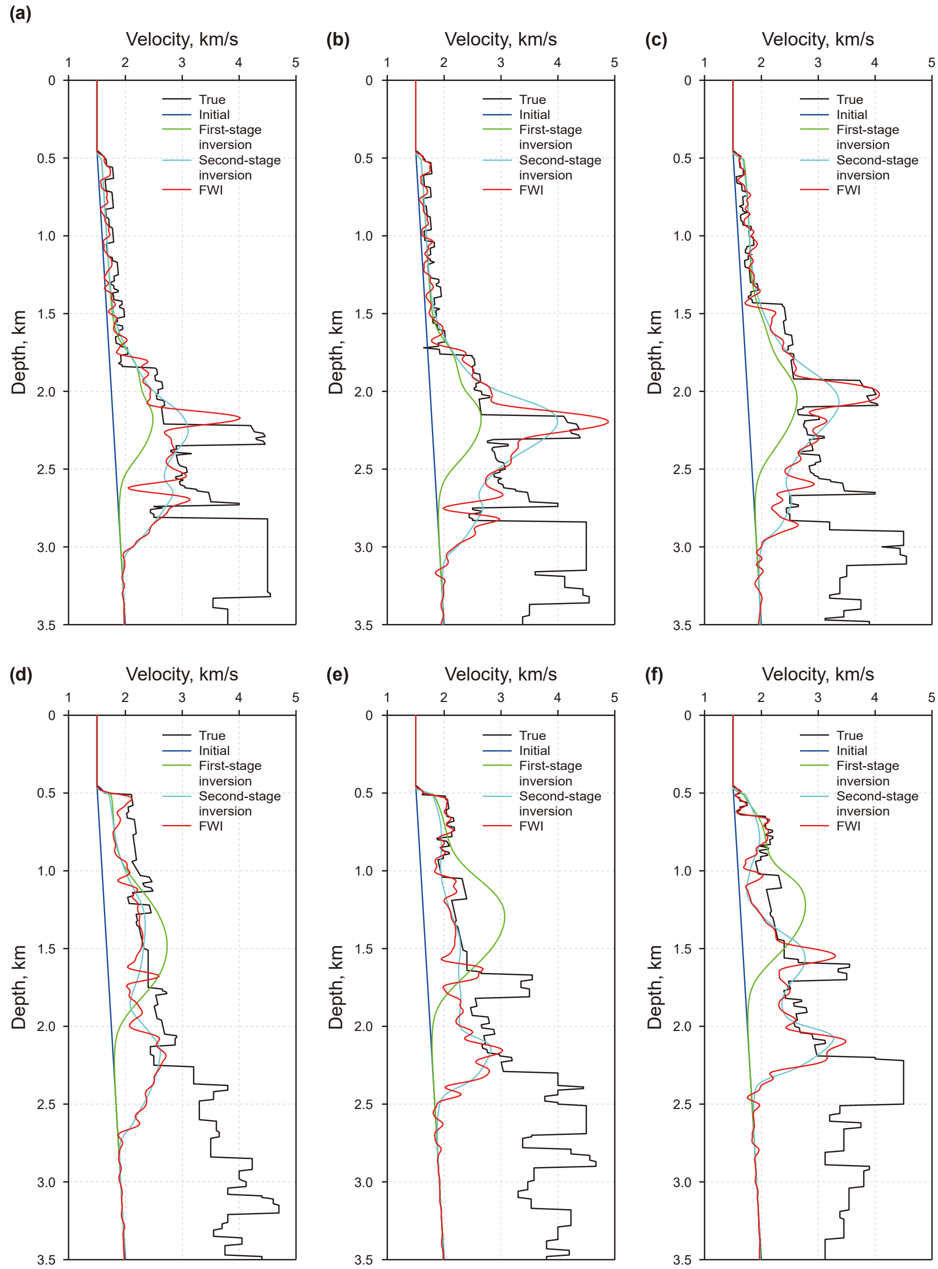

Fig. 29. Vertical velocity profile comparisons at surface locations: **(a)** 1.0 km; **(b)** 4.0 km; **(c)** 7.0 km; **(d)** 10.0 km; **(e)** 13.0 km; and **(f)** 16.0 km. Blue lines denote the initial model; black lines denote the true velocity; green and cyan lines represent the results after the first-stage and second-stage inversions, respectively; red lines represent the result after full waveform inversion.

5.4. Field data test

We further validate the proposed method using field data from an exploration area in eastern China. The prestack seismic data have undergone conventional preprocessing, and a representative shot gather is shown in Fig. 30, where clear reflection events can be observed. The initial velocity model, provided by the operating oil company, is shown in Fig. 31(a). Six characteristic reflectors are selected for inversion.

During the inversion, strong smoothing is applied to the gradient to retain only low-to intermediate-wavenumber components of the velocity model. The inverted velocity model is shown in Fig. 31(b). The corresponding migrated CIGs and stacked images obtained using the initial and inverted velocity models are shown in Figs. 32 and 33, respectively. Compared to the initial results, the CIGs after inversion are significantly flattened, and the migrated images are better focused and more coherent, demonstrating a clear improvement in imaging quality.

For field data, particular attention is paid to the practical implementation strategy of the proposed method. Given the limited bandwidth, incomplete offset coverage, and unavoidable noise in real seismic data, strong spatial smoothing is applied to

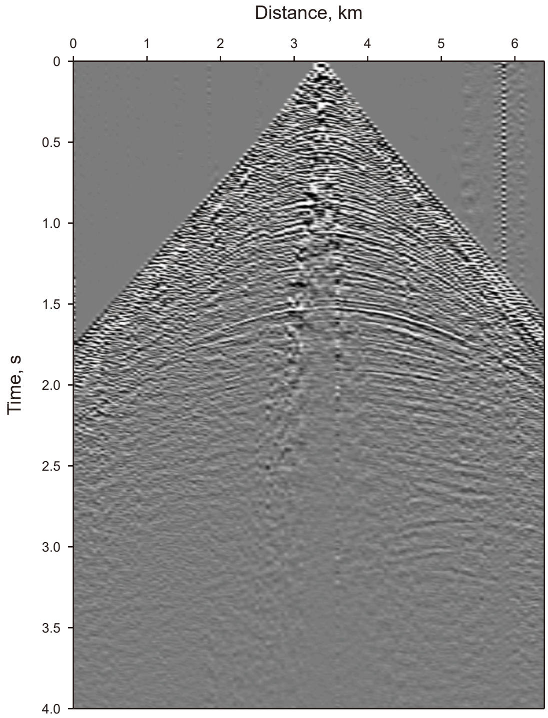

Fig. 30. Common-shot gather of the field data.

the gradient to retain only low-to intermediate-wavenumber components of the velocity update, which is consistent with the objective of background model building. Characteristic reflectors are manually picked by experienced interpreters based on image continuity and signal-to-noise ratio, ensuring meaningful reflector selection and reliable traveltime shift measurements in practical data conditions. The resulting velocity updates lead to significantly flatter common-image gathers and improved reflector focusing, indicating a better alignment between the velocity model and reflection kinematics. These observations suggest that the proposed method can be effectively integrated into practical seismic processing workflows, where it serves as a robust intermediate step between conventional migration velocity analysis and full waveform inversion.

6. Discussion

The proposed characteristic reflection-guided full-gradient traveltime inversion is designed to address the long-standing coupling between background velocity and reflectivity in reflection-based velocity inversion. Compared with time-consistent wave-equation inversion (TWIN), the present method differs both conceptually and practically. While TWIN resolves velocity-reflectivity coupling through a consistency term based on zero-offset (ZO) post-stack migration, requiring a separate ZO imaging treatment, our approach is formulated entirely within a unified two-way wave-equation framework. Wave propagation paths are controlled through angle selection derived from the Poynting vector under a small-angle constraint, avoiding reliance on ZO data that may be missing or incomplete in practice. Moreover, the required wavefield gradients are naturally available during two-way wavefield extrapolation, enabling a consistent derivation of full-gradient expressions. In contrast to one-way waveform inversion (OWI) approaches that treat velocity-reflector coupling in a one-way framework, the present method maintains physical consistency by treating wave propagation and gradient computation in a fully two-way setting. Another key distinction lies in the adjoint-source construction: the proposed method employs traveltime-based adjoint sources derived from cross-correlation measurements, rather than waveform-amplitude residuals. This choice yields improved convexity and stability for background velocity updates, particularly when the initial model is far from the true solution. The additional gradient term is driven by a newly defined imaging response that explicitly encodes traveltime mismatches; this response diminishes and ultimately vanishes as traveltime errors are corrected, ensuring physically meaningful and self-terminating velocity updates.

The effectiveness of the proposed method also depends on the selection of characteristic reflectors, which are used to guide the inversion. In this study, characteristic reflectors are manually picked following clear physical criteria: priority is given to strong, laterally continuous reflections that control background velocity variations; reflectors are selected sparsely and introduced progressively from dominant to secondary features. This strategy allows the inversion to proceed in multiple stages, gradually enriching the reflection information while maintaining stability. Although automatic horizon picking in complex geological settings remains challenging-especially in the presence of faults, strong noise, or multiples-existing machine-learning- and image-processing-based methods may be integrated in future work. From a computational perspective, the proposed method requires the computation of seven wavefields per iteration, compared with four in conventional reflection waveform inversion, resulting in an approximately 1.75-fold increase in per-iteration cost. However, this moderate overhead is offset by a substantial reduction in the number of required iterations, particularly when characteristic reflection constraints are applied. The synthetic and field data examples demonstrate that the method efficiently recovers low-to intermediate-wavenumber background velocity trends and provides a reliable foundation for subsequent FWI refinement. While extension to fully three-dimensional problems remains

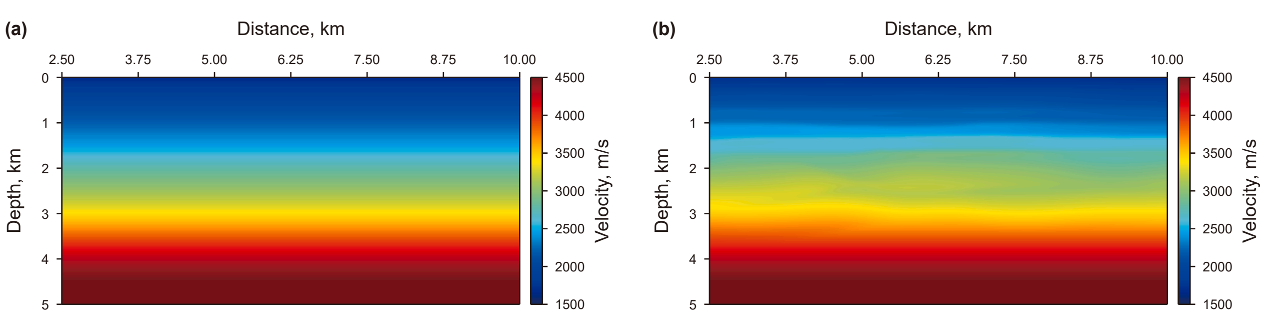

Fig. 31. (**a**) The initial velocity model and (**b**) the inverted velocity model.

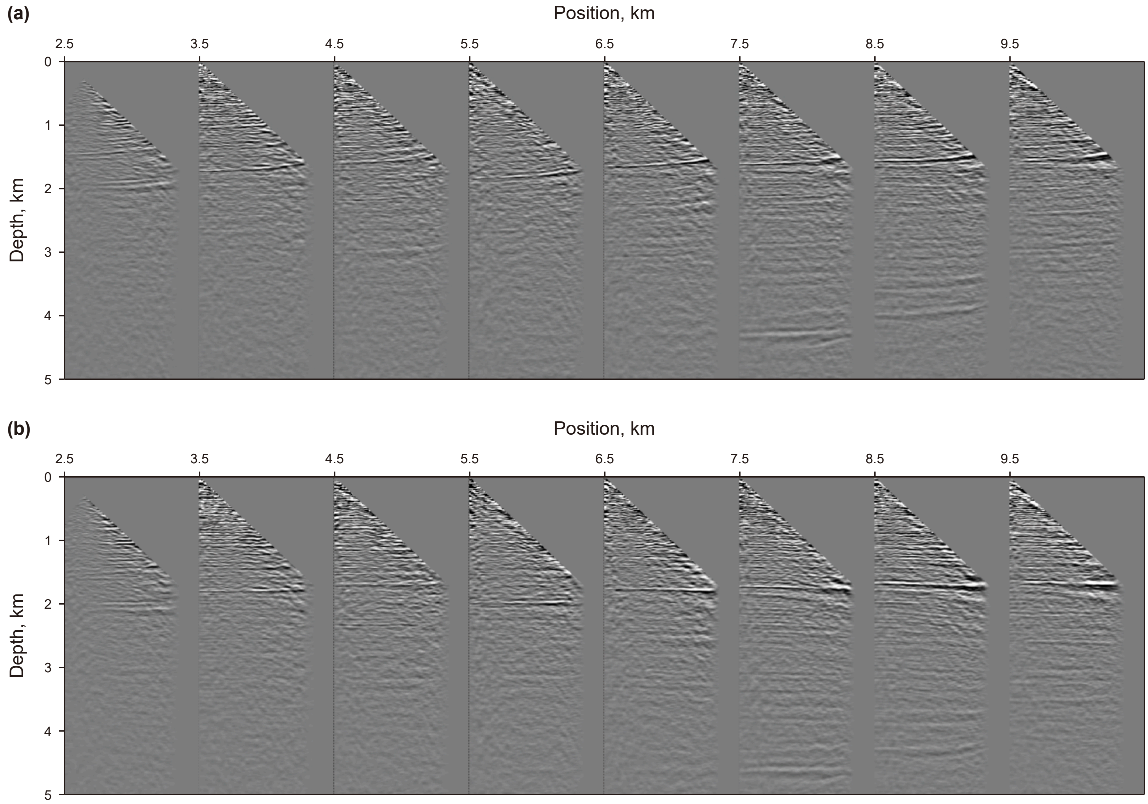

Fig. 32. CIGs generated using **(a)** the initial model; **(b)** the inverted model.

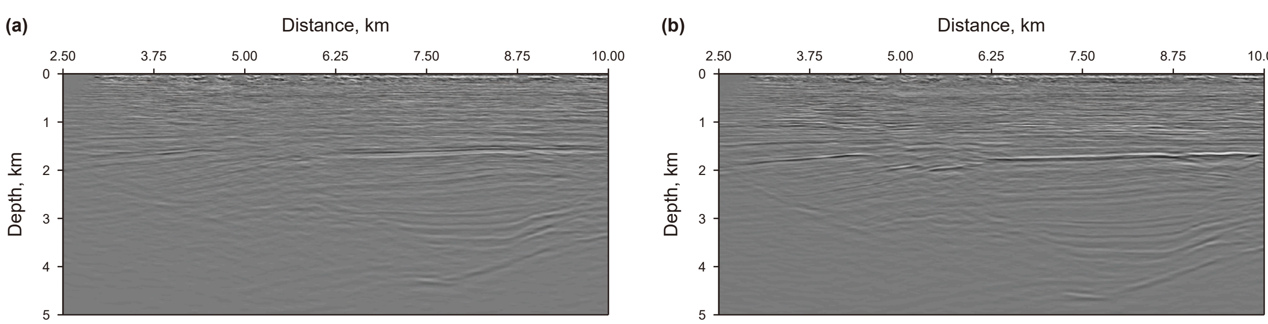

Fig. 33. Migration result obtained using **(a)** the initial velocity model, **(b)** the inverted model.

computationally demanding, ongoing work explores wavefield decomposition strategies to mitigate the cost of repeated wavefield extrapolations, as well as semi-automatic approaches for reflector selection in 3D datasets. Overall, the proposed framework effectively bridges reflection-based velocity analysis and waveform inversion, offering a robust and physically consistent pathway for background velocity model building in both synthetic and real-data applications.

7. Conclusion

Reflection traveltime inversion is a primary approach for velocity model updating in deep and ultra-deep exploration scenarios. However, reflection data are jointly influenced by both the background velocity and the reflector. In this paper, we propose a full-gradient reflection traveltime inversion method using characteristic reflection wavefields (CRWs) under the wave equation framework. We first reviewed the limitations of conventional reflection-based velocity modeling, where the velocity model and reflectivity are updated alternately. Then, based on the migration-demigration invariance of small-offset data, we derived the full gradient of the objective function with respect to the background velocity model. Subsequently, we extracted observed CRWs constrained by the characteristic reflector structure and developed a full-gradient-based inversion method tailored for CRWs. Numerical experiments validate the effectiveness of the proposed method. The results demonstrate that the full-gradient formulation improves inversion convergence and accuracy, enabling more reliable velocity model updates in complex geological settings.

CRediT authorship contribution statement

Cheng-Liang Wu: Writing – review & editing, Writing – original draft, Methodology, Conceptualization. **Bo Feng:** Writing – review & editing, Methodology, Conceptualization. **Hua-Zhong Wang:** Writing – review & editing, Methodology, Conceptualization.

Declaration of competing interest

The authors declare that they have no known competing financial interests or personal relationships that could have appeared to influence the work reported in this paper.

Acknowledgment

The authors thank the sponsors of the WPI group for their financial support and help. WPI's research works are also financially supported by the National Natural Science Foundation of China (Grant Nos. 42304124, 42574148, 42474142). Thanks to the RIPED and BGP of CNPC; Geophysical Research Institute of Shengli Oilfield, Geophysical Research Institute (Nanjing) and its Northwest Branch of SINOPEC; Research Institute and Zhanjiang Branch of CNOOC for their funding.

Appendix A

The cross-correlation function between observed and simulated reflection wavefields is defined as:

$$f(\mathbf{x}_\mathrm{r}, \mathbf{x}_\mathrm{s}, \tau) = \int d_\mathrm{obs}(\mathbf{x}_\mathrm{r}, t+\tau, \mathbf{x}_\mathrm{s}) d_\mathrm{cal}(\mathbf{x}_\mathrm{r}, t, \mathbf{x}_\mathrm{s}) \mathrm{d}t, \tag{A.1}$$

where f reaches its maximum when the $\tau = \Delta t(\mathbf{x}_\mathrm{r}, \mathbf{x}_\mathrm{s})$ corresponding to the traveltime shift of the target reflection event:

$$\Delta t(\mathbf{x}_\mathrm{r}, \mathbf{x}_\mathrm{s}) = \underset{\tau}{\mathrm{argmax}} \{ f(\mathbf{x}_\mathrm{r}, \mathbf{x}_\mathrm{s}, \tau) | \ \tau \in [-T_1, T_2] \}, \tag{A.2}$$

where T_1 and T_2 is the local time window.

From Eq. (A.1), the condition for the cross-correlation function to reach its maximum is

$$F(\Delta t) = \frac{\partial f(\mathbf{x}_\mathrm{r}, \mathbf{x}_\mathrm{s}, \tau)}{\partial \tau}\Big|_{\tau=\Delta t} = \int \dot{d}_\mathrm{obs}(\mathbf{x}_\mathrm{r}, t+\Delta t, \mathbf{x}_\mathrm{s}) d_\mathrm{cal}(\mathbf{x}_\mathrm{r}, t, \mathbf{x}_\mathrm{s}) \mathrm{d}t = 0. \tag{A.3}$$

Based on Eq. (A.3), the Fréchet derivative of the traveltime perturbation with respect to the velocity model can be written as,

$$\frac{\partial \Delta t}{\partial m_\mathrm{s}(\mathbf{x})} = -\frac{F_{m_\mathrm{s}(\mathbf{x})}}{F_{\Delta t}} = -\frac{\partial \dot{f}(\mathbf{x}_\mathrm{r}, \mathbf{x}_\mathrm{s}, \Delta t)}{\partial m_\mathrm{s}(\mathbf{x})} \left(\frac{\partial \dot{f}(\mathbf{x}_\mathrm{r}, \mathbf{x}_\mathrm{s}, \Delta t)}{\partial \Delta t} \right)^{-1}. \tag{A.4}$$

$$\frac{\partial \dot{f}(\mathbf{x}_\mathrm{r}, \mathbf{x}_\mathrm{s}, \Delta t)}{\partial \Delta t} = \int \ddot{d}_\mathrm{obs}(\mathbf{x}_\mathrm{r}, t+\Delta t, \mathbf{x}_\mathrm{s}) d_\mathrm{cal}(\mathbf{x}_\mathrm{r}, t, \mathbf{x}_\mathrm{s}) \mathrm{d}t. \tag{A.5}$$

$$\frac{\partial \dot{f}(\mathbf{x}_\mathrm{r}, \mathbf{x}_\mathrm{s}, \Delta t)}{\partial m_\mathrm{s}(\mathbf{x})} = \int \dot{d}_\mathrm{obs}(\mathbf{x}_\mathrm{r}, t+\Delta t, \mathbf{x}_\mathrm{s}) \frac{\partial u_\mathrm{cal}(\mathbf{x}_\mathrm{r}, t, \mathbf{x}_\mathrm{s})}{\partial m_\mathrm{s}(\mathbf{x})} \mathrm{d}t. \tag{A.6}$$

Based on Eq. (A.3), the Fréchet derivative of the traveltime perturbation with respect to the reflectivity can be expressed as,

$$\frac{\partial \Delta t}{\partial R(\mathbf{x})} = -\frac{F_{R(\mathbf{x})}}{F_{\Delta t}} = -\frac{\partial \dot{f}(\mathbf{x}_\mathrm{r}, \mathbf{x}_\mathrm{s}, \Delta t)}{\partial R(\mathbf{x})} \left(\frac{\partial \dot{f}(\mathbf{x}_\mathrm{r}, \mathbf{x}_\mathrm{s}, \Delta t)}{\partial \Delta t} \right)^{-1}. \tag{A.7}$$

$$\frac{\partial \dot{f}(\mathbf{x}_\mathrm{r}, \mathbf{x}_\mathrm{s}, \Delta t)}{\partial \Delta t} = \int \ddot{d}_\mathrm{obs}(\mathbf{x}_\mathrm{r}, t+\Delta t, \mathbf{x}_\mathrm{s}) d_\mathrm{cal}(\mathbf{x}_\mathrm{r}, t, \mathbf{x}_\mathrm{s}) \mathrm{d}t. \tag{A.8}$$

$$\frac{\partial \dot{f}(\mathbf{x}_\mathrm{r}, \mathbf{x}_\mathrm{s}, \Delta t)}{\partial R(\mathbf{x})} = \int \dot{d}_\mathrm{obs}(\mathbf{x}_\mathrm{r}, t+\Delta t, \mathbf{x}_\mathrm{s}) \frac{\partial u_\mathrm{cal}(\mathbf{x}_\mathrm{r}, t, \mathbf{x}_\mathrm{s})}{\partial R(\mathbf{x})} \mathrm{d}t. \tag{A.9}$$

Appendix B

We decompose the subsurface medium model $m(\mathbf{x})$ into a background parameter model $m_0(\mathbf{x})$ and a perturbation model $R(\mathbf{x})$:

$$m(\mathbf{x}) = m_0(\mathbf{x}) + R(\mathbf{x}). \tag{B.1}$$

The seismic wavefield is decomposed into a background wavefield $u_0(\mathbf{x}, t, \mathbf{x}_\mathrm{s})$ propagating in the background medium and a scattered wavefield $u_\mathrm{s}(\mathbf{x}, t, \mathbf{x}_\mathrm{s})$ resulting from the perturbation in the medium:

$$u(\mathbf{x}, t, \mathbf{x}_\mathrm{s}) = u_0(\mathbf{x}, t, \mathbf{x}_\mathrm{s}) + u_\mathrm{s}(\mathbf{x}, t, \mathbf{x}_\mathrm{s}). \tag{B.2}$$

Under the first-order Born approximation, the first-order reflection can be generated by the interaction of the incident background wavefield with the reflectivity:

$$\begin{cases} \left(m_0(\mathbf{x}) \dfrac{\partial^2}{\partial t^2} - \nabla^2 \right) u_0(\mathbf{x}, t, \mathbf{x}_\mathrm{s}) = f(t)\delta(\mathbf{x}-\mathbf{x}_\mathrm{s}) \\ \left(m_0(\mathbf{x}) \dfrac{\partial^2}{\partial t^2} - \nabla^2 \right) u_\mathrm{s}(\mathbf{x}, t, \mathbf{x}_\mathrm{s}) = -R(\mathbf{x}) \dfrac{\partial^2 u_0(\mathbf{x}, t, \mathbf{x}_\mathrm{s})}{\partial t^2} \end{cases}. \tag{B.3}$$

Eq. (B.3) is commonly referred to as the demigration wave equation. The integral form of Eq. (B.3) is given by

$$u_\mathrm{s}(\mathbf{x}, t, \mathbf{x}_\mathrm{s}) = -\int \frac{\partial^2 u_0(\mathbf{x}', t, \mathbf{x}_\mathrm{s})}{\partial t^2} * g_0(\mathbf{x}, t, \mathbf{x}') R(\mathbf{x}') \mathrm{d}\mathbf{x}', \tag{B.4}$$

where $g_0(\mathbf{x}, t, \mathbf{x}')$ denotes the Green's function in the background medium:

$$\left(m_0(\mathbf{x}) \frac{\partial^2}{\partial t^2} - \nabla^2 \right) g_0(\mathbf{x}, t, \mathbf{x}') = \delta(t)\delta(\mathbf{x}-\mathbf{x}'), \tag{B.5}$$

$$u_0(\mathbf{x}, t, \mathbf{x}_\mathrm{s}) = f(t) * g_0(\mathbf{x}, t, \mathbf{x}_\mathrm{s}). \tag{B.6}$$

Substituting Eq. (B.5) into Eq. (B.4), we obtain

$$u_\mathrm{s}(\mathbf{x}, t, \mathbf{x}_\mathrm{s}) = -\int f(t) * \frac{\partial g_0(\mathbf{x}', t, \mathbf{x}_\mathrm{s})}{\partial t^2} * g_0(\mathbf{x}, t, \mathbf{x}') R(\mathbf{x}') \mathrm{d}\mathbf{x}'. \tag{B.7}$$

Let $\ddot{g}_0(\mathbf{x}', t, \mathbf{x}_\mathrm{s}) = \frac{\partial g_0(\mathbf{x}', t, \mathbf{x}_\mathrm{s})}{\partial t^2}$, then the above equation becomes

$$u_\mathrm{s}(\mathbf{x}, t, \mathbf{x}_\mathrm{s}) = -\int f(t) * \ddot{g}_0(\mathbf{x}', t, \mathbf{x}_\mathrm{s}) * g_0(\mathbf{x}, t, \mathbf{x}') R(\mathbf{x}') \mathrm{d}\mathbf{x}'. \tag{B.8}$$

According to the relationship between the Green's function and the wavefield, the first-order reflection Green's function can be written as

$$g_s(\mathbf{x}, t, \mathbf{x}_s) = -\int \ddot{g}_0(\mathbf{x}', t, \mathbf{x}_s) * g_0(\mathbf{x}, t, \mathbf{x}') R(\mathbf{x}') \mathrm{d}\mathbf{x}'. \tag{B.9}$$

Assume the background velocity model $m_0(\mathbf{x})$ undergoes a small perturbation $\delta m_0(\mathbf{x})$,

$$m_s(\mathbf{x}) = m_0(\mathbf{x}) + \delta m_0(\mathbf{x}). \tag{B.10}$$

(a) This perturbation $\delta m_0(\mathbf{x})$ leads to a small change $\delta u_0(\mathbf{x}, t, \mathbf{x}_s)$ in the background wavefield. The Fréchet derivative of the background wavefield with respect to the background velocity can be expressed as

$$\frac{\partial u_0(\mathbf{x}, t, \mathbf{x}_s)}{\partial m_s(\mathbf{x})} = -\int f(t) * \ddot{g}_0(\mathbf{x}', t, \mathbf{x}_s) * g_0(\mathbf{x}, t, \mathbf{x}') \mathrm{d}\mathbf{x}'. \tag{B.11}$$

Thus, the Fréchet derivative of the Green's function with respect to the background velocity is

$$\frac{\partial g_0(\mathbf{x}, t, \mathbf{x}_s)}{\partial m_s(\mathbf{x})} = -\int \ddot{g}_0(\mathbf{x}', t, \mathbf{x}_s) * g_0(\mathbf{x}, t, \mathbf{x}') \mathrm{d}\mathbf{x}'. \tag{B.12}$$

(b) This perturbation $\delta m_0(\mathbf{x})$ also causes a variation $\delta u_s(\mathbf{x}, t, \mathbf{x}_s)$ in the reflection wavefield. The Fréchet derivative of the first-order reflection with respect to the background velocity is

$$\begin{aligned}\frac{\partial u_s(\mathbf{x}, t, \mathbf{x}_s)}{\partial m_s(\mathbf{x})} = & -\int f(t) * \frac{\partial \ddot{g}_0(\mathbf{x}', t, \mathbf{x}_s)}{\partial m_s(\mathbf{x}')} * g_0(\mathbf{x}, t, \mathbf{x}') R(\mathbf{x}') \mathrm{d}\mathbf{x}' \\ & -\int f(t) * \ddot{g}_0(\mathbf{x}', t, \mathbf{x}_s) * \frac{\partial g_0(\mathbf{x}, t, \mathbf{x}')}{\partial m_s(\mathbf{x}')} R(\mathbf{x}') \mathrm{d}\mathbf{x}'.\end{aligned} \tag{B.13}$$

Substituting Eq. (B.12) into Eq. (B.13) yields

$$\begin{aligned}\frac{\partial u_s(\mathbf{x}, t, \mathbf{x}_s)}{\partial m_s(\mathbf{x})} = & \int\int f(t) * \ddot{g}_0(\mathbf{y}, t, \mathbf{x}_s) * g_0(\mathbf{x}', t, \mathbf{y}) * \ddot{g}_0(\mathbf{x}, t, \mathbf{x}') R(\mathbf{y}) \mathrm{d}\mathbf{x}' \mathrm{d}\mathbf{y} \\ & + \int\int f(t) * \ddot{g}_0(\mathbf{x}', t, \mathbf{x}_s) * g_0(\mathbf{y}, t, \mathbf{x}') * \ddot{g}_0(\mathbf{x}, t, \mathbf{y}) R(\mathbf{y}) \mathrm{d}\mathbf{x}' \mathrm{d}\mathbf{y}.\end{aligned} \tag{B.14}$$

Substituting Eq. (B.9) into Eq. (B.14), the Fréchet derivative of the first-order reflection with respect to the background velocity becomes

$$\begin{aligned}\frac{\partial u_s(\mathbf{x}, t, \mathbf{x}_s)}{\partial m_s(\mathbf{x})} = & -\int f(t) * \ddot{g}_s(\mathbf{x}', t, \mathbf{x}_s) * g_0(\mathbf{x}, t, \mathbf{x}') d\mathbf{x}' \\ & -\int f(t) * \ddot{g}_0(\mathbf{x}', t, \mathbf{x}_s) * g_s(\mathbf{x}, t, \mathbf{x}') \mathrm{d}\mathbf{x}'.\end{aligned} \tag{B.15}$$

$$\begin{aligned}\frac{\partial u_s(\mathbf{x}, t, \mathbf{x}_s)}{\partial m_s(\mathbf{x})} = & -\int \ddot{u}_0(\mathbf{x}', t, \mathbf{x}_s) * g_s(\mathbf{x}, t, \mathbf{x}') d\mathbf{x}' \\ & -\int \ddot{u}_s(\mathbf{x}', t, \mathbf{x}_s) * g_0(\mathbf{x}, t, \mathbf{x}') \mathrm{d}\mathbf{x}'.\end{aligned} \tag{B.16}$$

(c) Based on Eq. (B.7), the Fréchet derivative of the first-order reflection with respect to the perturbation is

$$\frac{\partial u_s(\mathbf{x}, t, \mathbf{x}_s)}{\partial R(\mathbf{x})} = -\int f(t) * \ddot{g}_0(\mathbf{x}', t, \mathbf{x}_s) * g_0(\mathbf{x}, t, \mathbf{x}') \mathrm{d}\mathbf{x}'. \tag{B.17}$$

Or in an equivalent form:

$$\frac{\partial u_s(\mathbf{x}, t, \mathbf{x}_s)}{\partial R(\mathbf{x})} = -\int \ddot{u}_0(\mathbf{x}', t, \mathbf{x}_s) * g_0(\mathbf{x}, t, \mathbf{x}') \mathrm{d}\mathbf{x}'. \tag{B.18}$$

Appendix C

The characteristic reflectors $S(\mathbf{x})$ are obtained through the following process:

$$d_{\mathrm{obs}}(\mathbf{x}_r, t, \mathbf{x}_s) \overset{\text{migration}}{\to} I(\mathbf{x}, \mathbf{h}) \overset{\text{stack}}{\to} I(\mathbf{x}) \to S(\mathbf{x}), \tag{C.1}$$

where $I(\mathbf{x}, \mathbf{h})$ denotes the common-image gathers (CIGs), and $I(\mathbf{x})$ represents the stacked image.

The observed CRWs $\mathbf{d}^c_{\mathrm{obs}}$ is constructed by CRS-guided demigration applied to the CIGs,

$$I(\mathbf{x}, \mathbf{h}) \underset{S(\mathbf{x})}{\overset{\text{demigration}}{\to}} d^c_{\mathrm{obs}}(\mathbf{x}_r, t, \mathbf{x}_s). \tag{C.2}$$

The characteristic (CRS-guided) receiver wavefield $\mathbf{u}^c_r$ is then obtained as

$$u^c_r(\mathbf{x}, t, \mathbf{x}_r) = g_s(\mathbf{x}, t, \mathbf{x}_r) * d^c_{\mathrm{obs}}(\mathbf{x}_r, t, \mathbf{x}_s). \tag{C.3}$$

The characteristic background adjoint wavefield $p^c_s(\mathbf{x}, t, \mathbf{x}_r)$ and the characteristic reflection adjoint wavefield $p^c_r(\mathbf{x}, t, \mathbf{x}_r)$ are generated as follows:

$$p^c_s(\mathbf{x}, t, \mathbf{x}_r) = \sum_r \int y^c(\mathbf{x}_r, t, \mathbf{x}_s) * g_s(\mathbf{x}, t, \mathbf{x}_r) \mathrm{d}t, \tag{C.4}$$

$$p^c_r(\mathbf{x}, t, \mathbf{x}_r) = \sum_r \int y^c(\mathbf{x}_r, t, \mathbf{x}_s) * g_0(\mathbf{x}, t, \mathbf{x}_r) \mathrm{d}t. \tag{C.5}$$

The traveltime-mismatch imaging condition is defined as:

$$\tilde{I}^c(\mathbf{x}) = u_0(\mathbf{x}, t, \mathbf{x}_s) p^c_r(\mathbf{x}, t, \mathbf{x}_r). \tag{C.6}$$

The characteristic virtual reflected wavefield and the reverse-time-propagated characteristic virtual receiver wavefield are then generated by

$$q^c_r(\mathbf{x}, t, \mathbf{x}_r) = \sum_{\mathbf{x}'} -g_0(\mathbf{x}, t, \mathbf{x}') \tilde{I}^c(\mathbf{x}') * \ddot{u}^c_r(\mathbf{x}', t, \mathbf{x}_r), \tag{C.7}$$

$$q^c_s(\mathbf{x}, t, \mathbf{x}_s) = \sum_{\mathbf{x}'} -g_0(\mathbf{x}, t, \mathbf{x}') \tilde{I}^c(\mathbf{x}') * \ddot{u}_0(\mathbf{x}', t, \mathbf{x}_s). \tag{C.8}$$

This appendix summarizes the construction of CRS-guided wavefields and adjoint variables used in the full-gradient formulation, providing a complete and reproducible description of the CRS-based implementation.

References

Abolhassani, S., Hoogerbrugge, L., Verschuur, D.J., 2025. One-way reflection waveform inversion with depth-dependent gradient pre-conditioning. Geophys. J. Int. 240 (1), 652–672. https://doi.org/10.1093/gji/ggae397.
Abreo, S., Ramirez, A., Vivas, F., et al., 2018. Diving-wave FWI methodology applied to a Colombian Caribbean data set. Lead. Edge 37 (4), 291–295. https://doi.org/10.1190/tle37040291.1.
Alkhalifah, T., 2014. Scattering-angle based filtering of the waveform inversion gradients. Geophys. J. Int. 200 (1), 363–373. https://doi.org/10.1093/gji/ggu379.
Alkhalifah, T., Wu, Z., 2016. Multiscattering inversion for low-model wavenumbers. Geophysics 81 (6), R417–R428. https://doi.org/10.1190/geo2015-0650.1.

Assis, C.A.M., Chauris, H., Audebert, F., et al., 2024. Investigating Hessian-based inversion velocity analysis. Geophysics 89 (2), R169–R186. https://doi.org/10.1190/geo2022-0689.1.
Baina, R., Valensi, R., 2018. Borrowing insight from travel-time reflection tomography to solve the depth reflectivity-velocity coupling issue of RFWI. In: EAGE Technical Program Expanded Abstracts 2018, cp-556-00013. https://doi.org/10.3997/2214-4609.201801886.
Borisov, D., Miller, R.D., Sloan, S.D., 2025. Optimal transport-based full-waveform inversion for shallow seismic data. Geophysics 90 (3), R101–R112. https://doi.org/10.1190/geo2024-0165.1.
Brossier, R., Operto, S., Virieux, J., 2015. Velocity model building from seismic reflection data by full-waveform inversion. Geophys. Prospect. 63 (2), 354–367. https://doi.org/10.1111/1365-2478.12190.
Bunks, C., Saleck, F.M., Zaleski, S., et al., 1995. Multiscale seismic waveform inversion. Geophysics 60 (5), 1457–1473. https://doi.org/10.1190/1.1443880.
Chavent, G., 2017. Data space reflectivity and the migration based travel time approach to FWI. In: EAGE Technical Program Expanded Abstracts 2017, cp-519-00060. https://doi.org/10.3997/2214-4609.201701710.
Chavent, G., Gadylshin, K., Tcheverda, V., 2014. Full waveform inversion in migration based travel-time formulation. In: 6th EAGE Saint Petersburg International Conference and Exhibition, cp-20140198. https://doi.org/10.3997/2214-4609.20140198.
Chen, G.X., Wu, R.S., Chen, S.C., 2018. Reflection multi-scale envelope inversion. Geophys. Prospect. 66 (7), 1258–1271. https://doi.org/10.1111/1365-2478.12624.
Chen, H., Zhou, H., Rao, Y., 2020. Source wavefield reconstruction in fractional Laplacian viscoacoustic wave equation-based full waveform inversion. IEEE Trans. Geosci. Rem. Sens. 59, 6496–6509. https://doi.org/10.1109/TGRS.2020.3029630.
Cheng, X., Xu, J., Vigh, D., et al., 2023. Enhanced template matching full-waveform inversion. In: EAGE Technical Program Expanded Abstracts 2023, cp-202310765. https://doi.org/10.3997/2214-4609.202310765.
da Silva, S.L., Costa, F., Karsou, A., et al., 2024. Research note: Application of refraction full-waveform inversion of ocean bottom node data using a squared-slowness model parameterization. Geophys. Prospect. 72 (3), 1189–1195. https://doi.org/10.1111/1365-2478.13454.
Fichtner, A., Trampert, J., Cupillard, P., et al., 2013. Multiscale full waveform inversion. Geophys. J. Int. 194 (1), 534–556. https://doi.org/10.1093/gji/ggt118.
Hassine, A.B., Duprat, V., Baina, R., et al., 2022. One-way waveform inversion (OWI). In: EAGE Technical Program Expanded Abstracts 2022, cp-202210632. https://doi.org/10.3997/2214-4609.202210632.
Hassine, A.B., Duprat, V., Baina, R., et al., 2024. One-way waveform inversion: Real marine data application. Geophys. Prospect. 72 (6), 2087–2108. https://doi.org/10.1111/1365-2478.13498.
Hu, Y., Han, L., Xu, Z., et al., 2017. Adaptive multi-step full waveform inversion based on waveform mode decomposition. J. Appl. Geophys. 139, 195–210. https://doi.org/10.1016/j.jappgeo.2017.02.017.
Huang, G., Nammour, R., Symes, W., 2017. Full-waveform inversion via source-receiver extension. Geophysics 82 (3), R153–R171. https://doi.org/10.1190/geo2016-0301.1.
Huang, Y., Mao, J., Sheng, J., et al., 2023. Toward high-fidelity imaging: Dynamic matching FWI and its applications. Lead. Edge 42 (2), 124–132. https://doi.org/10.1190/tle42020124.1.
Irabor, K., Warner, M., 2016. Reflection FWI. In: SEG Technical Program Expanded Abstracts 2016, pp. 1136–1140. https://doi.org/10.1190/segam2016-13944219.1.
Kang, W., Brand, N., Cheng, X., et al., 2021. Reliability, efficiency, and robustness: Enhanced template-matching full-waveform inversion using sparse ocean-bottom node data. In: EAGE Technical Program Expanded Abstracts 2021, cp-202112566. https://doi.org/10.3997/2214-4609.202112566.
Kazei, V., Tessmer, E., Alkhalifah, T., 2016. Scattering angle-based filtering via extension in velocity. In: SEG Technical Program Expanded Abstracts 2016, pp. 1157–1162. https://doi.org/10.1190/segam2016-13870908.1.
Kryvohuz, M., Kuehl, H., Plessix, R.-É., et al., 2019. Reflection full-waveform inversion with data-space LSRTM. In: SEG Technical Program Expanded Abstracts 2019, pp. 1229–1233. https://doi.org/10.1190/segam2019-3216501.1.
Lee, K.H., Kim, H.J., 2003. Source-independent full-waveform inversion of seismic data. Geophysics 68 (6), 2010–2015. https://doi.org/10.1190/1.1635054.
Li, Y.E., Demanet, L., 2016. Full-waveform inversion with extrapolated low-frequency data. Geophysics 81 (6), R339–R348. https://doi.org/10.1190/geo2016-0038.1.
Liu, Y., He, B., Lu, H., et al., 2018. Full-intensity waveform inversion. Geophysics 83 (6), R649–R658. https://doi.org/10.1190/geo2017-0682.1.
Luo, Y., Schuster, G.T., 1991. Wave-equation traveltime inversion. Geophysics 56 (5), 645–653. https://doi.org/10.1190/1.1443081.
Mao, J., Sheng, J., Huang, Y., et al., 2020. Multi-channel dynamic matching full-waveform inversion. In: SEG Technical Program Expanded Abstracts 2020, pp. 666–670. https://doi.org/10.1190/segam2020-3427610.1.
Nie, Z., Feng, B., Wang, H., et al., 2025. Multi-scale full waveform inversion based on gradient bidimensional empirical mode decomposition. Geophysics 90 (5), R285–R296. https://doi.org/10.1190/geo2024-0267.1.
Plessix, R., Milcik, P., Corcoran, C., et al., 2012. Full waveform inversion with a pseudotime approach. In: EAGE Technical Program Expanded Abstracts 2012, cp-293-00717. https://doi.org/10.3997/2214-4609.20148713.
Qu, Y., Li, Z., Huang, J., et al., 2017. Elastic full-waveform inversion for surface topography. Geophysics 82 (5), R269–R285. https://doi.org/10.1190/geo2016-0349.1.
Ramos-Martinez, J., Crawley, S., Zou, K., et al., 2016. A robust gradient for long wavelength FWI updates. In: ASEG Extended Abstracts 2016, cp- 201601536. https://doi.org/10.1071/ASEG2016ab133.
Sun, D., Jiao, K., Cheng, X., et al., 2016. Reflection-based waveform inversion. In: SEG Technical Program Expanded Abstracts 2016, pp. 1151–1156. https://doi.org/10.1190/segam2016-13966097.1.
Tarantola, A., 1984. Inversion of seismic reflection data in the acoustic approximation. Geophysics 49 (8), 1259–1266. https://doi.org/10.1190/1.1441754.
Tcheverda, V., Chavent, G., Gadylshin, K., 2016. Macrovelocity reconstruction by reflection FWI. In: EAGE Technical Program Expanded Abstracts 2016, cp-Th SRS2 06. https://doi.org/10.3997/2214-4609.201601539.
Valensi, R., Baina, R., 2019. On the reflectivity-velocity coupling issue in the RFWI method. In: SEG Technical Program Expanded Abstracts 2019, pp. 1234–1238. https://doi.org/10.1190/segam2019-3216528.1.
Valensi, R., Baina, R., 2021. A time consistent waveform inversion (TWIN) method. In: EAGE Technical Program Expanded Abstracts 2021, cp-202113295. https://doi.org/10.3997/2214-4609.202113295.
Valensi, R., Baina, R., Duprat, V., 2017. Reflection waveform inversion method: Solutions to the reflectivity-background coupling problem and consequences on the convergence. In: EAGE Technical Program Expanded Abstracts 2017, pp. 519–500070. https://doi.org/10.3997/2214-4609.201701720.
Van Leeuwen, T., Mulder, W., 2009. A variable projection method for waveform inversion. In: 71st EAGE Conference and Exhibition Incorporating SPE EUROPEC 2009, pp. 127–374. https://doi.org/10.3997/2214-4609.201400381.
Vandrasi, V., Al-Waily, M., Mothi, S., et al., 2020. Time-lag FWI based velocity model and image of a coarse shallow water OBC data set. In: SEG Technical Program Expanded Abstracts 2020, pp. 715–719. https://doi.org/10.1190/segam2020-3427971.1.
Vigh, D., Cheng, X., Jiao, K., et al., 2019. Is the salt-related full-waveform inversion sorted out?. In: SEG Technical Program Expanded Abstracts 2019, pp. 1265–1269. https://doi.org/10.1190/segam2019-3215741.1.
Virieux, J., Operto, S., 2009. An overview of full-waveform inversion in exploration geophysics. Geophysics 74 (6), WCC1–WCC26. https://doi.org/10.1190/1.3238367.
Wang, L., Min, F., Pan, S., et al., 2024. FWI-WF: robust full-waveform inversion using hybrid Wasserstein-1 and Fourier metrics. Geophysics 89 (6), F117–F128. https://doi.org/10.1190/geo2024-0056.1.
Wang, M., Xie, Y., Deng, P., et al., 2023. Dynamic resolution TLFWI for velocity model building beyond the reach of diving waves. In: EAGE Technical Program Expanded Abstracts 2023, cp-202310637. https://doi.org/10.3997/2214-4609.202310637.
Wang, P., Zhang, Z., Mei, J., et al., 2019. Full-waveform inversion for salt: A coming of age. Lead. Edge 38 (3), 204–213. https://doi.org/10.1190/tle38030204.1.
Wang, S., Chen, F., Zhang, H., et al., 2013. Reflection-based full waveform inversion (RFWI) in the frequency domain. In: SEG Technical Program Expanded Abstracts 2013, pp. 877–881. https://doi.org/10.1190/segam2013-0671.1.
Wang, T., Cheng, J., Geng, J., 2021. Reflection full waveform inversion with second-order optimization using the adjoint-state method. J. Geophys. Res. Solid Earth 126 (8). https://doi.org/10.1029/2021JB022135 e2021JB022135.
Wu, C., Feng, B., Song, X., et al., 2023a. Automatic horizon picking using multiple seismic attributes and Markov decision process. Remote Sens. 15, 552. https://doi.org/10.3390/rs15030552.
Wu, C., Feng, B., Wang, H., et al., 2023b. An effective scheme for residual moveout picking using a Markov decision process. IEEE Trans. Geosci. Rem. Sens. 61, 1–11. https://doi.org/10.1109/TGRS.2023.3306339.
Wu, C., Wang, H., Feng, B., et al., 2025. High-resolution stacking image based on common-image gathers. Geophysics 90 (4), S101–S114. https://doi.org/10.1190/geo2024-0358.1.
Wu, C., Wang, H., Feng, B., et al., 2024. Characteristic reflection wavefield-based wave equation traveltime inversion. Geophysics 89 (5), R457–R477. https://doi.org/10.1190/geo2024-0029.1.
Xie, C., Qin, Z.L., Wang, J.H., et al., 2024. Full waveform inversion based on hybrid gradient. Pet. Sci. 21 (3), 1660–1670. https://doi.org/10.1016/j.petsci.2024.01.013.
Xu, S., Wang, D., Chen, F., et al., 2012a. Inversion on reflected seismic wave. In: SEG Technical Program Expanded Abstracts 2012. https://doi.org/10.1190/segam2012-1473.1 cp-SEG-2012-1473.
Xu, S., Wang, D., Chen, F., et al., 2012b. Full waveform inversion for reflected seismic data. In: EAGE Technical Program Expanded Abstracts 2012, cp-293-00729. https://doi.org/10.3997/2214-4609.20148725.
Xu, W., Wang, T., Cheng, J., et al., 2021. Hessian-based reflection waveform inversion: Theory and applications to synthetic and field data. Geophysics 86 (5), R747–R762. https://doi.org/10.1190/geo2020-0601.1.
Yan, J., Dickens, T.A., 2016. Reverse time migration angle gathers using poynting vectors. Geophysics 81 (6), S511–S522. https://doi.org/10.1190/geo2015-0703.1.
Yang, Y., Ramos-Martinez, J., Whitmore, N.D., et al., 2020. FWI using reflections for deep velocity model updates. In: SEG Technical Program Expanded Abstracts 2020, pp. 691–695. https://doi.org/10.1190/segam2020-3427709.1.
Yao, G., Wu, D., Wang, S.X., 2020. A review on reflection-waveform inversion. Pet. Sci. 17 (2), 334–351. https://doi.org/10.1007/s12182-020-00431-3.

Yoon, K., Marfurt, K.J., 2006. Reverse-time migration using the Poynting vector. Explor. Geophys. 37 (1), 102–107. https://doi.org/10.1071/EG06102.
Zhang, K., Wang, H., Li, Z., et al., 2025. Reflection waveform inversion based on Wasserstein-2 distance. J. Appl. Geophys. 238, 105722. https://doi.org/10.1016/j.jappgeo.2025.105722.
Zhang, P., Han, L., Xu, Z., et al., 2017. Sparse blind deconvolution based low-frequency seismic data reconstruction for multiscale full waveform inversion. J. Appl. Geophys. 139, 91–108. https://doi.org/10.1016/j.jappgeo.2017.02.021.
Zhang, Z., Mei, J., Lin, F., et al., 2018. Correcting for salt misinterpretation with full-waveform inversion. In: SEG Technical Program Expanded Abstracts 2020, pp. 1143–1147. https://doi.org/10.1190/segam2018-2997711.1.
Zhou, W., Brossier, R., Operto, S., et al., 2015. Full waveform inversion of diving & reflected waves for velocity model building with impedance inversion based on scale separation. Geophys. J. Int. 202 (3), 1535–1554. https://doi.org/10.1093/gji/ggv228.